

1 **Earthquake-induced landslides in Haiti: analysis of**
2 **seismotectonic and possible climatic influences**

3

4 Hans-Balder Havenith¹, Kelly Guerrier², Romy Schlögel^{1,3}, Anika Braun⁴, Sophia
5 Ulysse^{2,5}, Anne-Sophie Mreyen⁶, Karl-Henry Victor², Newdeskarl Saint-Fleur², Lena
6 Cauchie¹, Dominique Boisson², Claude Prépetit⁵

7

8 ¹University of Liege, Department of Geology, Georisk and Environment, Liege, 4000, Belgium

9 ²Université d'Etat d'Haïti, Faculté des Sciences, LMI-CARIBACT, URGéo, Port-au-Prince, Haiti

10 ³Centre Spatial de Liège, Liege, 4000, Belgium

11 ⁴TU Berlin, Faculty VI Planning Building, Environment Department of Engineering Geology, Berlin,
12 1587, Germany

13 ⁵Unité Technique de Sismologie, Bureau des Mines et de l'Energie, Port-au-Prince, Delmas 31, Haiti

14 ⁶University of Liege, Department of Urban & Environmental Engineering, Applied Geophysics, Liege,
15 4000, Belgium

16

17 Correspondence to: Hans-Balder Havenith (hb.havenith@uliege.be)

18

19

20

21

22

23

24 **Abstract.** First analyses of landslide distribution and triggering factors are presented for the region
25 affected by the August, 14, 2021, earthquake ($M_w=7.2$) in the Nippes Department, Haiti. Landslide
26 mapping was mainly carried out by comparing pre- and post-event remote imagery (~0.5 -1-m resolution)
27 available on Google Earth Pro® and Sentinel-2 (10-m resolution) satellite images. The first covered
28 about 50% of the affected region (for post-event imagery and before completion of the map in January
29 2022), the latter were selected to cover the entire potentially affected zone. On the basis of the completed
30 landslide inventory, comparisons are made with catalogues compiled by others both for the August 2021
31 and the January 2010 seismic events, including one open inventory (by the United States Geological
32 Survey) that was also used for further statistical analyses. Additionally, we studied the pre-2021
33 earthquake slope stability conditions. These comparisons show that the total number of landslides
34 mapped for the 2021 earthquake (7091) is larger than the one recently published by another research
35 team for the same event, but it is also clearly smaller than the one observed by two other research teams
36 for the 2010 earthquake (e.g., 23,567, for the open inventory). However, these apparently fewer
37 landslides triggered in 2021 cover much wider areas of slopes ($>80 \text{ km}^2$) than those induced by the 2010
38 event ($\sim 25 \text{ km}^2$ – considering the open inventory). A simple statistical analysis indicates that the lower
39 number of 2021-landslides can be explained by the missing detection of the smallest landslides triggered
40 in 2021, partly due to the lower resolution imagery available for most of the areas affected by the recent
41 earthquake; this is also confirmed by an inventory completeness analysis based on size-frequency
42 statistics. The much larger total area of landslides triggered in 2021, compared to the 2010 earthquake,
43 can be related to different physical reasons: a) the larger earthquake magnitude in 2021; b) the more
44 central location of the fault segment that ruptured in 2021 with respect to coastal zones; c) and possible
45 climatic preconditioning of slope instability in the 2021-affected area. These observations are supported
46 by (1) a new pre-2021 earthquake landslide map, (2) rainfall distribution maps presented for different
47 periods (including October 2016 - when Hurricane Matthew had crossed the western part of Haiti),
48 covering both the 2010 and 2021 affected zones, as well as (3) shaking intensity prediction maps.

49 **1 Introduction**



50 This paper presents a first overview of landslides induced by the August 14, 2021, Nippes (Haiti)

51 earthquake. The epicenter (18.434° N / 73.482° W, hypocentral depth of 10 km) of this event is located
52 in the western part of the southern Haitian peninsula (see Unites States Geological Survey, USGS,
53 Earthquake Hazard Program page, earthquake.usgs.gov, presenting first information on the 2021 M 7.2
54 - Nippes, Haiti, event). Similar to the January 12, 2010, earthquake, the epicenter is located near the
55 surface expression of the Enriquillo-Plantain-Garden Fault (EPGF) that crosses the peninsula from east
56 to west, marking one of the highest seismic hazard zones of the island (see location of the epicenters on
57 the seismic hazard map completed by Frankel et al. in 2011 in Fig. A1 in the annex, as well as on the
58 topographic map shown in Fig. 1).

59 For the 2010 event, Calais et al. (2010) and Symithe et al. (2013) showed that this earthquake was caused
60 by the oblique rupture of a formerly unknown fault dipping towards the north and located immediately
61 in the north of the EPGF. Data provided by the earthquake.usgs.gov webpage (considering the provided
62 moment tensor solution; see also Okuwaki and Fan, 2022) indicate that the situation could be similar for
63 the 2021 event, with a ruptured fault segment dipping towards the north, and mostly located in the north
64 of the EPGF. Thus, also the recently ruptured fault segment would not belong to the EPGF (which is
65 essentially a left-lateral strike-slip fault). It could be related to an adjacent blind fault segment with
66 oblique slip character (left-lateral strike-slip combined with reverse movement) according to the
67 information available on earthquake.usgs.gov, and to Okuwaki and Fan (2022). The latter further indicate
68 that especially the eastern part of the ruptured fault showed a more reverse while the western part a
69 preferential strike-slip mechanism. However, by now there is still no clear answer to the question related
70 to the fault itself. Therefore, below we will use the term of the 'EPGF zone' that includes the main strike-
71 slip fault and annexed oblique (or combined) slip fault segments (the two that are now known, i.e., the
72 one ruptured in 2010 and the one that produced the last earthquake) to denominate the tectonic structure
73 that produced those two events.

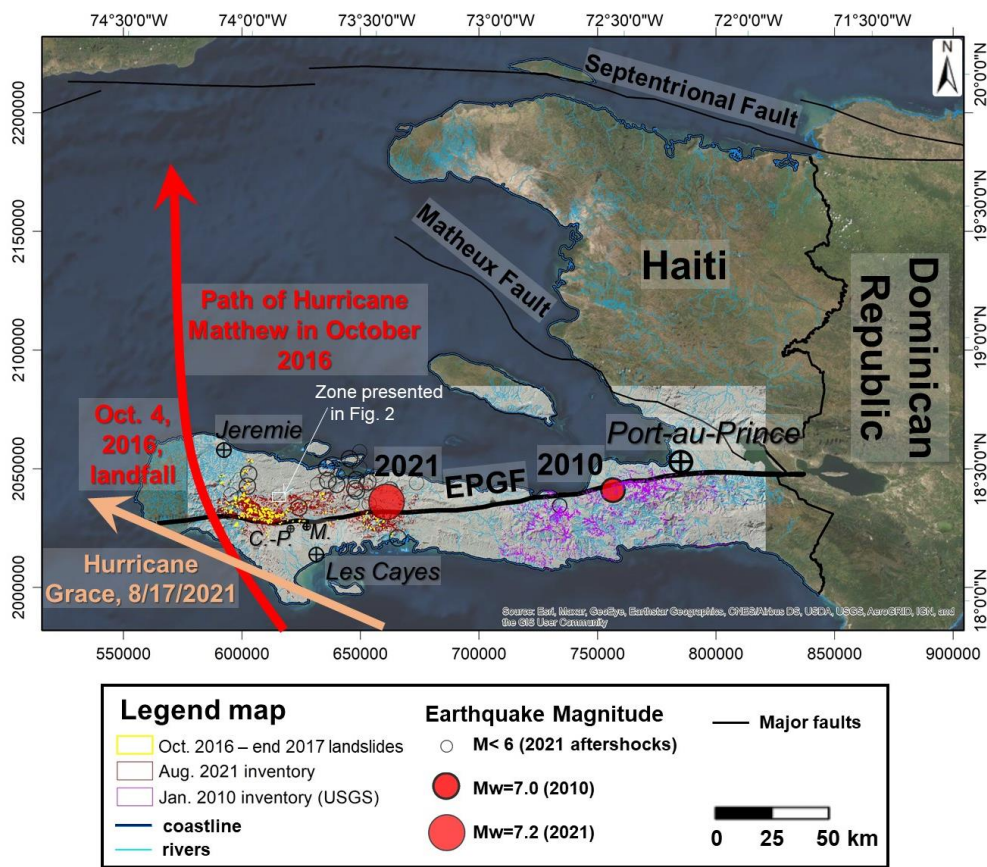
74 Even though the magnitude of the 2021 earthquake is slightly larger than the one of 2010 (Mw=7.2 and
75 Mw=7.0, respectively, see information on the earthquake.usgs.gov webpage and by Stein et al., 2021),
76 the recent event was far less catastrophic as it hit a less populated area compared to the 2010 earthquake
77 that occurred just near the western entrance of the capital of Haiti, Port-au-Prince. The 2021 earthquake
78 accounts for about 2250 fatalities (2/3 of which occurred in the provincial city of Les Cayes, located in
79 Fig. 1), while the 2010 death toll is up to 300,000. However, it quickly became clear that the last event

80 caused widespread slope failures that could be more intense than in 2010. Therefore, members of our
81 research team completed some ground control during a one-week field visit along segments of important
82 roads hit by rock falls near the epicentral region. Additionally, we mapped landslides over the whole area
83 potentially hit by the 2021 event by using satellite imagery of variable resolution, as it will be explained
84 in section 2. The main target of this mapping task was to produce an input data set for an extensive
85 landslide susceptibility analysis that will be presented in an upcoming publication.

86 Such event-based seismically induced landslide inventories allow us to complete a more systematic
87 analysis of global patterns of those mass movements, such as size-frequency relationships (Malamud et
88 al., 2004; Tanyas et al., 2019b), estimates of the expected number of landslides and affected area
89 (Havenith et al., 2016; Keefer and Wilson, 1989; Marc et al., 2017), and very general earthquake-
90 triggered landslide susceptibility markers (Tanyas et al., 2019a). At regional scale, event-based landslide
91 inventories are valuable to understand more specific patterns of seismic slope instability, particularly
92 with respect to the earthquake mechanism and the geological and climatic context (Gorum et al., 2011;
93 Tanyas et al., 2022). Below, we will also present statistical characteristics of this new 2021 inventory
94 compared with equivalent results obtained for the 2010 USGS landslide catalogue published by Harp et
95 al. (2016); some statistical data are also compared with those of the other inventory completed by
96 Martinez et al. (2021, USGS Open File report) for the 2021 event and of two additional catalogues
97 compiled for the 2010 event (by Gorum et al., 2013 and Xu et al., 2014).

98 Finally, we also mapped landslides existing before the 2021 earthquake by using high-resolution (≤ 1
99 m) imagery available on Google Earth Pro®, starting from October 2014 until the end of 2017, to study
100 some preconditioning of slope instability that was induced in 2021. In particular, it is known that the
101 region is often affected by hurricanes – the last catastrophic one, ‘Matthew’ ~~or ‘Mathieu’ in French~~, had
102 impacted the target area in October 2016. Also, just two days after the main shock, on August 16, another
103 Hurricane, ‘Grace’, hit the area and hampered help convoys to reach the areas most impacted by the
104 earthquake. Right after this event, it was not immediately clear if Grace had contributed to landslide
105 activity or not; this question will be analyzed in the following sections by comparing landslide
106 distributions with monthly precipitation maps produced by the ‘Global Precipitation Measurement’
107 (GPM) Mission (NASA) for different periods.

108 Fig. 1 presents an overview map with outlines of landslides mapped by Harp et al. (2016) (shown by
 109 light violet - pink polygons, near the 2010 M=7 epicenter), and the recently mapped landslides triggered
 110 in August 2021 (outlined in dark red, mainly in the west and south of the 2021 epicenter). This map also
 111 shows the approximate paths of the two aforementioned hurricanes near Haiti. Other digital outlines (also
 112 those presented in the following figures that also present more detailed views with more clearly visible
 113 outlines), such as roads, rivers, faults and coastline, were provided by the Centre National de
 114 l'Information Géo-Spatiale (CNIGS) of Haiti.



115
 116 **Figure 1: Location of the study region in Haiti: Satellite image view of Haiti (by © ESRI), with study region**
 117 **highlighted by the hillshade. See also location of the 2010 and 2021 epicenters, and the major cities (see also**
 118 **‘C.-P.’ for Camp-Perrin and ‘M.’ for Maniche) by hit by those two events. Outlines of major faults are shown**
 119 **as well as the indication of the approximate paths of Hurricane Matthew in October 2016 and of Hurricane**
 120 **Grace in August 2021. Landslides mapped by Harp et al. (2016) are shown by light violet polygons, and**
 121 **recently mapped landslides triggered in August 2021 are outlined in dark red See also location of the zone**
 122 **presented in Fig. 2.**

123

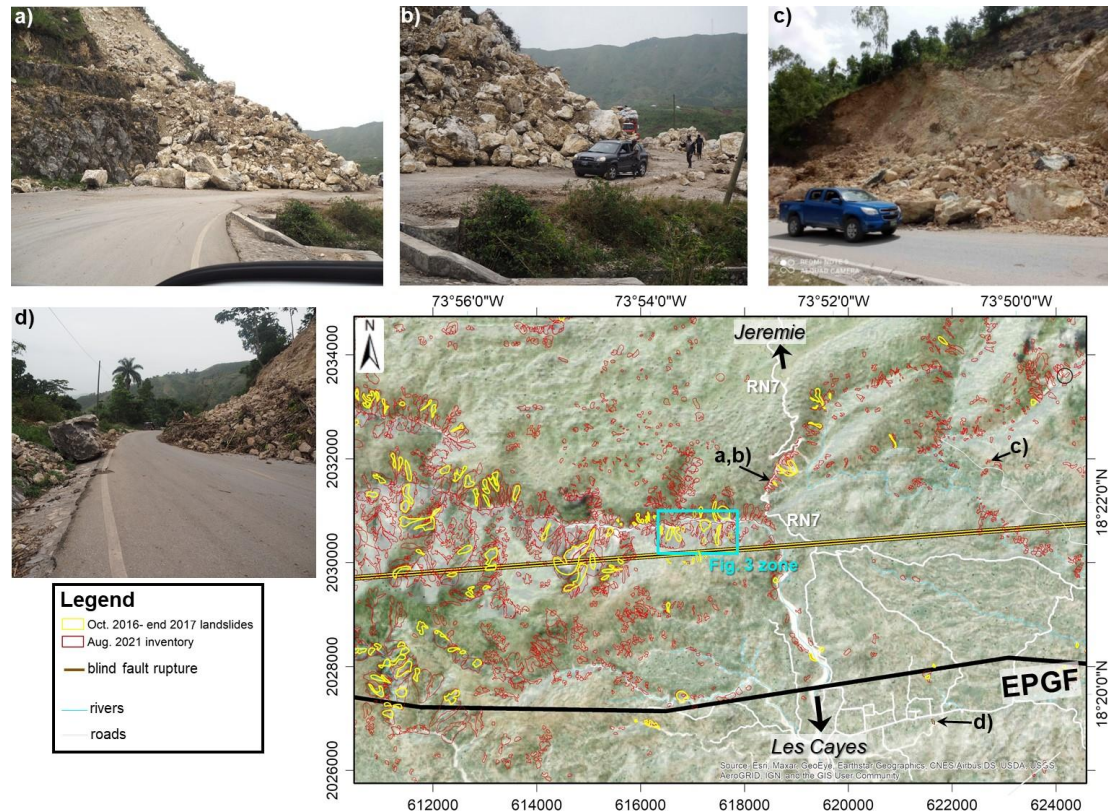
124 The following sections will provide more detail about the landslide mapping itself, the completion of
125 landslide statistics, the collection of climatic data and the computation of seismic intensity maps. All
126 those inputs will be used to explain both the common and the different main markers of landslide
127 catalogues, respectively, for the 2010 and the 2021 events.

128 **2 Methodological aspects of landslide and seismic trigger factor mapping**

129 **2.1 Landslide mapping**

130 2.1.1 Field observations

131 Right after the main shock that hit Haiti on August 14, 2021 (precisely at 12:29:08 UTC, about 8:30 am
132 local time), it became clear that many landslides were triggered by this earthquake. Within a few hours
133 after the main shock, there were reports about rock falls cutting the main road RN7 connecting the large
134 provincial cities of Les Cayes in the south and Jeremy in the north. Therefore, local members of our
135 research team checked the situation to support local administration with cleaning the roads. Photographs
136 of rock falls in the central part of the target area are shown in Fig. 2 (those shown below all occurred in
137 limestone rocks), together with the locations of the affected sites on a map.



138

139 **Figure 2: Examples of landslides photographed in the field, especially along the national road RN7, connecting**
 140 **the two provincial cities of Les Cayes in the south and Jeremie in the north. The map (semi-transparent**
 141 **hillshade on high-resolution satellite imagery, by © ESRI) also shows the different ground failure effects**
 142 **mapped before (yellow polygons) and after the earthquake (dark red polygons). See blue rectangle marking**
 143 **the outline of the view extent shown in Fig. 3 (and in Fig. A2).**

144


145 These rock falls were typically not very large (with a volume of generally less than 20,000 m³), but there
 146 were many of them and in some cases, it took several days before the street could be reopened. For that
 147 reason, we started to detect and map all landslides caused by the earthquake. In addition, during field
 148 visits in August 2021, just after the main shock, our teams could confirm that this earthquake had
 149 triggered more extensive slope failures (covering wider surface areas) than the previous M=7.0 event in
 150 January 2010.

151

152 2.1.2 Regional mapping of landslides using remote imagery of August – November 2021

153 Mapping of earthquake-induced landslides is often done from pre- and post-event optical and radar

154 satellite imagery, both publicly accessible, like Sentinel-2 (Tanyas et al., 2022) or Landsat-7 and -8 data,
155 with resolutions starting from 10 m, or commercial higher resolution data that is often made publicly
156 available for disaster response, through Google Earth, with resolutions of down to 0.5 m e.g. (Harp et al.,
157 2016; Kargel et al., 2016; Wartman et al., 2013). Sometimes mapping is also supported by (pre-event)
158 digital elevation data (Gorum et al., 2011; Kargel et al., 2016) or even by field or helicopter
159 reconnaissance. Landslides are mapped at different levels of spatial discretization, e.g. as landslide
160 initiation points (Gorum et al., 2011), centroid points (Wartman et al., 2013), or landslide polygons
161 (Tanyas et al., 2022), and with a varying degree of detail, e.g. regarding the minimum mapped landslide
162 size or the identification of landslide types. The quality and accuracy of the inventories depend typically
163 on the resolution of the satellite data, cloud cover, and the availability of suitable pre-event data for a
164 clear identification of co-seismic landslides. A recent review of earthquake-induced landslide inventories
165 was presented by Tanyas et al. (2017).

166 In our case, medium-resolution imagery available from the Copernicus Open-Access Hub was used for
167 the landslide mapping over the whole potentially affected area: Sentinel-2, with 10-m spatial resolution
168 bands B2 (490 nm), B3 (560 nm), B4 (665 nm) and B8 (842 nm) collected for eight different dates, every
169 five to six days, between August 14, 2021 (the first one was available about two hours after the main
170 shock), and the end of September 2021 (an example of a Sentinel 2 image view of this period is shown
171 in the annex, in Fig. A2a, presenting a view of the zone located in the map in Fig. 2). Analyzing all
172 images was necessary due to the extensive (but spatially variable) cloud cover present on each image.
173 Considering that only this medium-resolution imagery was freely available in the beginning, the authors
174 are aware that the landslides could not be mapped with the highest precision, and that not all er
175 landslides could be identified. However, during the following months, also higher resolution (0.5-1 m)
176 imagery became available on Google Earth Pro® (GEPPro) for about 50% of the potentially affected
177 region (before December 2021). For these areas, the initial landslide outlines could be refined, and also
178 smaller slope failures could be mapped; an example of the ‘resolution’ effect on landslide mapping is
179 shown in the annex, by Fig. A2, comparing the aforementioned Sentinel 2 image (black-white, projected
180 on the topography in GEPPro) with a higher resolution image of the same landslide zone that became
181 available on GEPPro in September 2021. On the basis of such comparisons between higher and lower
182 resolution imagery, we could see that most larger landslides are actually composed of multiple initially

183 smaller and narrower slides and flows, which had coalesced to form a larger coherent mass (while also
184 on the higher resolution imagery no clear separation could be outlined within this landslide area); actually,
185 the refinement could only help identify distinct sources of those larger mass movements, but the outline
186 of the main sliding mass often remained the same. Furthermore, for most landslide zones, no clear
187 distinction could be made between landslide scarp and deposits, as it can often be observed for such kind
188 of disrupted mass movements.

189

190 2.1.3 Regional mapping of landslides using remote imagery of November 2014 – August 2021, with
191 focus on pre-seismic changes that occurred in October 2016

192 For the entire area, also a comparison with pre-event imagery was completed to be sure that only ‘co-
193 seismic’ (or nearly co-seismic – see explanation below) slope failures had been mapped; this check was
194 especially necessary for the identification of the smaller co-seismic landslides. Therefore, the impacted
195 region was screened by using high resolution (0.5-1 m) imagery available on GEPro for the period
196 between 2014 and August 2021. A pre-earthquake image (of November 28, 2014) of the same landslide-
197 impacted area is shown in Fig. 3a, highlighting the contrast between the vegetated slopes present in the
198 target region and the extensive denudation that occurred during the earthquake of August 2021 (see
199 images shown in Fig. 3d, identical to the one shown in the annex in Fig. A2a). However, we could also
200 observe by comparing multiple images available for the pre-event period that some denudation had
201 already appeared for smaller zones before 2021. Zones marked by narrow debris slides and flows could
202 be outlined especially on images available for the time just after October 10, 2016. Fig. 3b presents an
203 image of October 12, 2016 that shows the ‘freshest’ type of denudation since 2014 (see yellow polygons
204 outlining such denudation zones), some of which disappeared after a few years (see Fig. 2c), due to
205 revegetation of the slopes (rapid revegetation can be observed as the whole area is located in tropical
206 regions). This image and others available for the same period were added to GEPro after Hurricane
207 Matthew had impacted, in early October 2016, the same area as the one hit by the 2021 earthquake. The
208 consequences of this ‘double’ impact on the target region will be analyzed in the sections 3 and 4 on the
209 basis of precipitation distribution maps.

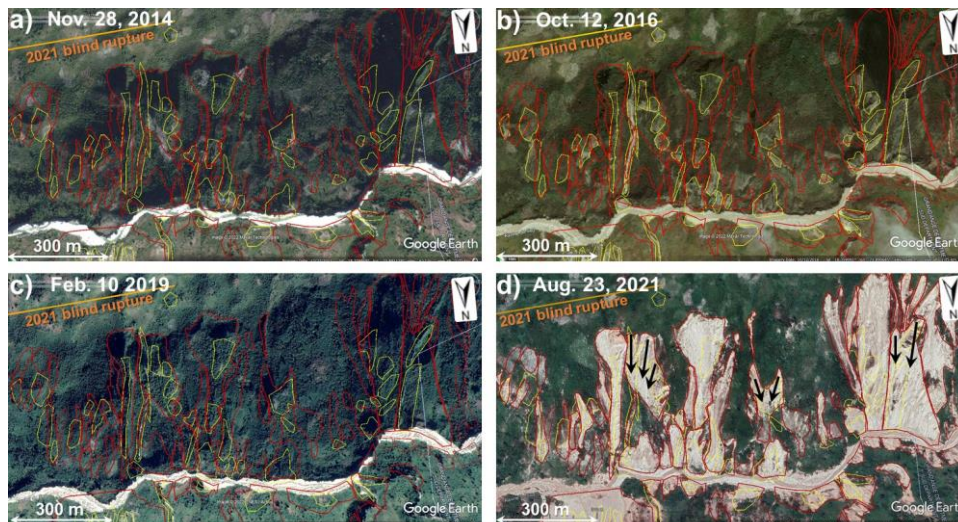
210 Actually, Haiti is quite often (at least once per year) crossed by hurricanes or severe tropical storms, some
211 of which can trigger slope failures over wide areas. One such tropical storm that later developed into the

212 hurricane called Grace had also crossed southern Haiti, just two to three days after the August 14, 2021,
213 main shock. We introduce this fact here in the methodological part as it had two consequences for the
214 landslide mapping: first, right after the earthquake wide areas were covered by clouds during several
215 days (some higher mountain parts even for weeks); thus, multiple satellite images of different dates (both
216 Sentinel-2 and higher resolution imagery on GEP had to be inspected to map landslides over the whole
217 area. Second, we had to consider that Grace might also have induced slope failures and that landslides
218 mapped by using post-hurricane imagery were not all seismically triggered, or were at least enlarged by
219 the effects of Grace. Therefore, by comparing the post-seismic, August 14, Sentinel-2 image (collected
220 before the Hurricane Grace event) with the one of August 29, 2021 (post-seismic and post-hurricane),
221 we checked if additional or enlarged slope failures had appeared on the latter. An example of such a
222 comparison is presented in Fig. A3, where red arrows point to zones marked larger slope failures on the
223 Sentinel-2 image of August 29, 2021, which were thus most likely reactivated by rainfall during the
224 Grace climatic event (discussing here the possible additional influence of aftershocks occurring at the
225 same time in the region). Unfortunately, due to the extensive cloud cover in mid-August 2021, such a
226 comparison could only be completed for about 10% of the seismically impacted area. For those cloud-
227 free zones, we estimate that Grace had only induced a widening of the initially seismically triggered
228 slope failures, but the importance of this reactivation process cannot be quantified due to the extensive
229 cloud cover and related shadow effects on the surface.

230

231

232



233

234 **Figure 3: Evolution of landslides within the zone marked in Fig. 2 between November 2014 (view a), after**
 235 **Hurricane Matthew (Oct. 2016, b), a view of the area of Feb. 2019 (c) and of Oct. 2021, about two months of**
 236 **the earthquake (an image of August exists, but it is partly cloudy). Landslides that occurred during or directly**
 237 **after the Hurricane Matthew event are outlined in yellow and those that were triggered by the August 14,**
 238 **2021, earthquake are shown by dark red polygons; see also black arrows marking the coalescence of landslides**
 239 **with distinct sources (only for three examples shown). Views on © Google Earth Pro.**

240

241 **2.2 Landslide distribution statistics, climatic context and a first size-frequency analysis**

242 In sub-section 3.2, observed total landslide numbers and surface areas as well as other parameters
 243 characterizing the statistics of the two inventories, the new one presented here for 2021 and the one for
 244 2010 by Harp et al. (2016), are compared with ‘predicted’ ones. The latter numbers are computed
 245 according to prediction laws proposed by Havenith et al. (2016) and Malamud et al. (2004). To estimate
 246 the total number (N_{LT} , see Eq. 1) of landslides triggered by a specific earthquake, Havenith et al. (2016)
 247 recommend to take into consideration the shaking intensity factor, (I , based on the Arias Intensity, see
 248 Arias (1970), and thus on the earthquake magnitude, M ; see Eq. 6b in the next sub-section), the fault
 249 factor F (depending on the type, FT , and size of the fault rupture, considering also the influence of a
 250 possible surface rupture), the topographic energy (TE , using mainly as parameter the maximum altitude
 251 difference in the affected region), the climatic background (CB) conditions, and the lithological factor
 252 (LF , depending on the presence of soft soils for instance). Related factor values used for the calculations

253 are compared with estimated minimum and maximum values in Table 2, in the following section.

$$254 \quad N_{LT} = 1000 \times I \times F \times TE \times CB \times LF , \quad (1)$$

255 Compared with the prediction of the total number of landslides triggered by a specific earthquake
256 proposed by Havenith et al. (2016), the one recommended by Malamud et al. (2004) is much simpler (Eq.
257 2) and only based on the earthquake magnitude, M .

$$258 \quad N_{LT} = 10^{(1.29M - 5.65)} , \quad (2)$$

259 For the calculation of the total area potentially affected by landslides (A_{Lext} , area within the maximum
260 extent of landslide occurrence, equivalent to the area of distribution defined by Marc et al., 2017, and
261 Tanyas and Lombardo, 2019) Havenith et al. (2016) propose the following Eq. (3), which also directly
262 considers the earthquake magnitude, M , and the hypocentral Depth, D :

$$263 \quad A_{Lext} = I \times FT \times TE \times CB \times LF \times M \times D^2 , \quad (3)$$

264 As Havenith et al. (2016), Keefer and Wilson (1989) also propose an equation to estimate the total area
265 potentially affected by landslides during one earthquake event. Their estimate of A_{Lext} is purely based on
266 the earthquake magnitude, similar to Eq. (2) proposed by Malamud et al. (2004) to estimate N_{LT} :

$$267 \quad A_{Lext} = 10^{(M - 3.46)} , \quad (4)$$

268 Malamud et al. (2004) do not propose any formula to estimate the total area potentially affected by
269 landslides during an earthquake event as Havenith et al. (2016) (see Eq. 3), but recommend the following
270 prediction law (Eq. 5) to estimate the total area effectively covered by co-seismic landslides, A_{LT} , based
271 on the observed or predicted (using Eq. 2, or any other related prediction law, such as the one in Eq. 1)
272 total number of landslides:

$$273 \quad A_{LT} = 0.00307 N_{LT} , \quad (5)$$

274 All the previous equations were used to compute the respective values presented in Table 1 in sub-section
275 3.2.

276 Size-frequency relations were computed for the 7091 landslide outlines in terms of frequency-density
277 function (FDF) on the basis of the measured surface areas, $f(A_L)$. The same statistics were also computed
278 for the 23,567 landslides mapped by Harp et al. (2016). Therefore, we used the method introduced by

279 Malamud et al. (2004) for surface areas (Eq. 6):

$$280 \quad f(A_L) = \frac{\delta N_L}{\delta A_L} \quad (6)$$

281 where δN_L is the number of landslides with areas between A_L and $A_L + \delta A_L$ (representing the difference
282 between two landslide surface area classes). Surface areas were calculated in km^2 . Related distributions
283 computed, respectively, for each landslide catalogue (for the 2010 one by Harp et al., 2016; and for the
284 new 2021 inventory) are then compared with theoretical frequency-density distributions, as proposed by
285 Malamud et al. (2004). The latter are based on the three-parameter inverse-gamma probability
286 distribution (see equation 3 in Malamud et al., 2004) that is multiplied by the total number of landslides
287 of simulated events (100, 1000, etc.). In this regard, it should be noted that the original technique
288 proposed by Malamud et al. (2004) to complete the size-frequency statistics is based on the probability-
289 density values, corresponding to the frequency-density values divided by the total number of mapped
290 landslides, N_{LT} (which can be fit by the aforementioned three-parameter inverse-gamma probability
291 distribution). However, as indicated above, due to the limited amount of high-resolution imagery
292 available for the area potentially affected by seismic shaking in August 2021, not all small landslides
293 could be mapped; therefore, the total number of landslides seismically triggered in August, N_{LT} , is likely
294 to be higher than 7091 (even if the potential ‘hurricane-effect’ is removed, as explained below), and the
295 probability-density function cannot be correctly computed. For such cases, Malamud et al. (2004)
296 recommend the computation of the frequency-density function to assess the completeness of the
297 inventory by comparison with the aforementioned predefined theoretical frequency-density functions, as
298 it will be shown for the 2010 and 2021 inventories in the following results section.

299 To provide information about the climatic context covering different periods of time, we used the Global
300 Precipitation Measurement Mission (GPM, by NASA) data obtained via the
301 <https://giovanni.gsfc.nasa.gov/> website, corresponding to the merged satellite-gauge monthly
302 precipitation estimate (in mm), assessed with a resolution of 0.1° . Related maps were extracted for all
303 months between August 2000 and July 2021, and also for the specific months of October 2016 and August
304 2021, as well as for all October months between 2000 and 2020. Note, we also extracted maps for shorter
305 periods around the climatic events of Matthew in 2016 and Grace in 2021, but those did not provide any
306 additional information. Additionally, we tried to support these merged satellite - rain gauge estimates by

307 additional ground measurement data. However, the *Centre National de l'Information Géo-Spatiale*,
308 *CNIGS*, of Haiti, informed us that such data would not be available; therefore, we can only rely on these
309 regional estimates.

310 **2.3 Mapping of seismic landslide triggering factors**

311 The aforementioned climatic data are supposed to help us better understand the pre-conditioning of slope
312 stability in the target area and thus will also be used below for the interpretation of the landslide
313 distribution statistics. However, it is obvious that for such an event the main trigger factors are still related
314 to earthquake shaking; those have to be assessed to understand why extensive slope instability could be
315 observed in one zone and only isolated minor failures occurred in another one. Such an analysis is
316 completed both for the 2010 and 2021 events, by computing the Arias Intensity distribution maps (for
317 2010, comparing the results with the landslide distribution as observed by Harp et al., 2016).

318 The Arias Intensity, I_a , can be considered as a quantitative measure of the degree of shaking (in m/s) on
319 the surface. With respect to any other intensity characterization (including the one based on surveys) it
320 has the advantage to be more objective and comparable for different earthquakes (according to Harp and
321 Wilson, 1995). Wilson and Keefer (1985) were the first to try to correlate seismically triggered landslide
322 distributions with this intensity measure. They also defined the following empirical attenuation
323 relationship (Eq. 7a) in terms of magnitude (M) and hypocentral distance (R):

$$324 \log(I_a) = -4.1 + M - 2 \log(R) + 0.5P , \quad (7a)$$

325 where P considers a possible deviation from the main law (P=0 stands for the average value).

326 Afterwards, Keefer and Wilson (1989) have reviewed the application of this formula and defined a new
327 one (Eq. 7b), for magnitudes greater than 7:

$$328 \log(I_a) = -2.35 + 0.75M - 2 \log(R) , \quad (7b)$$

329 We applied the latter equation as both the 2010 and 2021 can be considered as $M \geq 7$ events. The R-
330 value represents the hypocentral distance map, here computed by using as source zone the blind fault
331 rupture segments of the 2010 and 2021 events (with 0 km epicentral distance and 10 km hypocentral
332 depth along the respective segment; information extracted from earthquake.usgs.gov).

333 All equations introduced above have been applied to obtain the computation results presented below, in

334 the sub-sections 3.2 and 3.4.

335 **3 Results: landslide inventory statistics and analysis of trigger conditions**

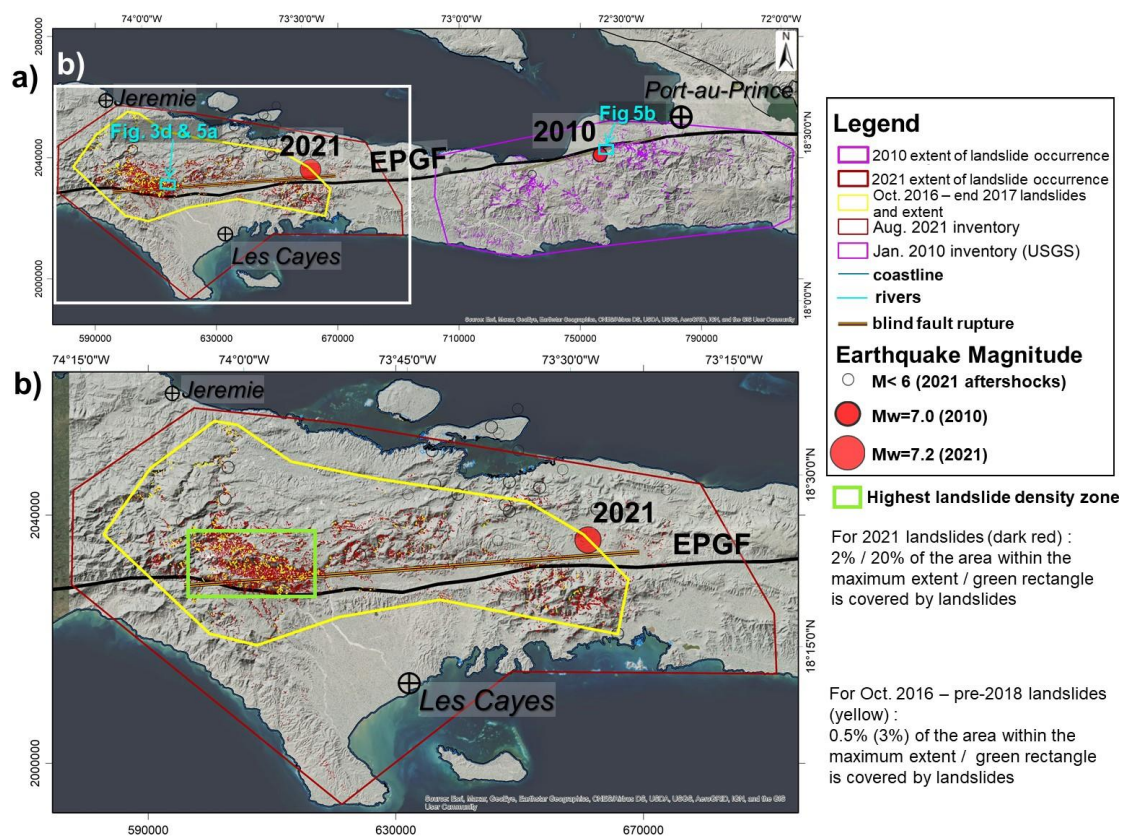
336 This section first summarizes a series of landslide type and general distribution characteristics. Second,
337 landslide inventory and size-frequency statistics are presented and supported by an inventory
338 completeness analysis. Third, a study of possible climatic slope failure preconditioning and post-seismic
339 landslide surface changes is presented, which also compares landslide distributions with monthly
340 precipitation maps (using output maps of the Global Precipitation Measurement Mission, GPM, produced
341 by the NASA, for different periods, according to Acker and Leptough, 2007). Fourth, the landslide
342 occurrence observed in 2010 and in 2021 is compared with respective shaking intensity prediction maps.

343 **3.1 Landslide type and distribution characteristics**

344 Before analyzing specific statistical values of the two landslide inventories, the one compiled by Harp et
345 al. (2016) for the 2010 event and ours completed after the August 2021 earthquake, we first have a look
346 at the general respective spatial landslide distributions and provide basic information on the type of the
347 mapped landslides.

348 The map presented in Fig. 4a shows that the global extent of landslides triggered in 2010 (pink outlines
349 within the pink maximum extent polygon) and in 2021 (dark red outlines within the dark red maximum
350 extent polygon) is quite similar (exact values are presented in Table 1). This map also show the location of
351 the main shock and aftershocks (empty circles, from earthquake.usgs.gov) and the outline of the (roughly 80 km
352 long) blind fault rupture (extracted from USGS page:
353 <https://earthquake.usgs.gov/earthquakes/eventpage/us6000f65h/finite-fault>). Outlines of zones shown in Fig. 5 are
354 shown by light blue rectangles. A major difference between the two landslide distributions can mainly be
355 observed with respect to the location of the EPGF zone. While most landslides occurred in the south of
356 the fault zone in 2010, a relatively symmetric distribution of landslides with respect to the location of the
357 EPGF zone can be observed for the 2021 event. This is mainly due to the fact that the fault segment that
358 ruptured near EPGF in 2010 is located close to the coast (actually just in the south of the coast, as can be
359 seen in the map in Fig. 4a), and thus only limited onshore surface areas could be affected by landslides

360 in the north of the EPGF zone in 2010, while the location of the fault segment that ruptured in 2021 is
 361 more central within the southwestern peninsula of Haiti (see focus on this region in Fig. 4b).
 362 Another important observation is that there seems to be a gap between the zone affected by landslides in
 363 2010 and the one affected in 2021. This means that, according to our present observations, the 2021
 364 earthquake did not reactivate landslides triggered in 2010 – due to the large distance (> 60 km) between
 365 the fault ruptures. However, it should be noted that this check could only be completed so far with the
 366 10-m resolution Sentinel-2 imagery. Now, we cannot exclude that very small landslides (that we cannot
 367 identify on Sentinel 2 imagery) triggered in 2010 had been reactivated in 2021.



368
 369 **Figure 4: a) Study region with areas affected, respectively, by the two Mw \geq 7 events. Individual landslides**
 370 **triggered in 2010 (Harp et al., 2016, inventory) and our landslides mapped for the 2021 earthquake and**
 371 **October 2016 hurricane events are shown, respectively, as pink, dark red and yellow polygons. The maximum**
 372 **extent of landslides triggered in 2010, in 2021 and 2016 is outlined, respectively, by the large pink, dark red,**
 373 **and yellow polygons. b) Focus on the region hit by the August 2021 earthquake, with 7091 landslide locations.**
 374 **Map background by © ESRI.**

375

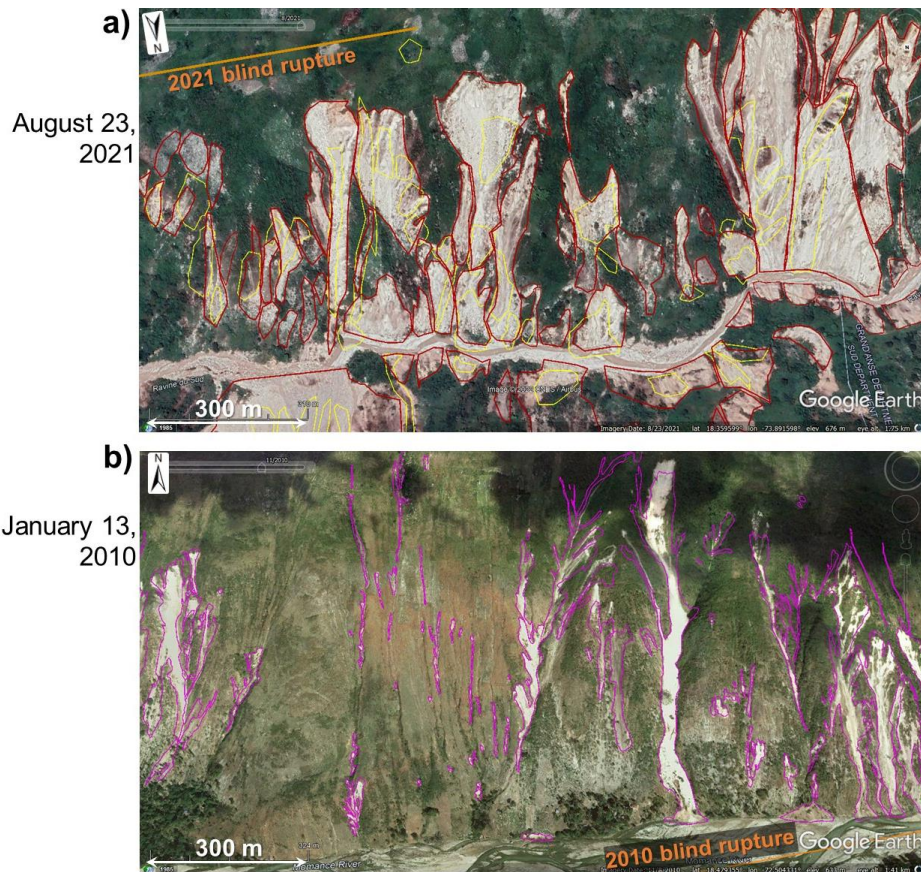
376 An important consequence of the specific location of the ruptured fault segments is that a few dozens of
377 landslides with a surface area larger than 2000 m² had occurred along the shore in 2010, where the two
378 or three largest ones (likely including an important submarine part) had massively impacted the ocean
379 and, thus, had produced up to 3 m-high tsunami waves (see Olson et al., 2011; Poupardin et al., 2020;
380 Fritz et al., 2013; Sassa and Takagawa, 2018) while there is not a single report of a major coastal landslide
381 for the 2021 event – as the fault rupture occurred at a distance of minimum 10 km away from the nearest
382 shoreline. Instead, a wider onshore area was exposed to high intensity earthquake shaking during the
383 2021 event. The related impact will be analyzed below on the basis of the statistical values presented in
384 Table 1.

385 Concerning the types of landslides triggered by the 2021 earthquake, we can say that by far most of them
386 can be classified as debris slides or flows (see examples in the GEPro view presented in Fig. 5a) and as
387 medium-size (most with a volume of less than 20,000 m³) rockfalls (as shown above in Fig. 2). Thus, we
388 estimate that at least 95% of all landslides mapped are relatively shallow (with a depth of less than 10
389 m). Actually, not a single large massive landslide (> 10⁷ m³) could be identified. A similar observation
390 was made by Harp et al. (2016) for the landslides triggered in 2010 (see view in Fig. 5b). However, when
391 comparing individual landslides induced in 2021 with those triggered in 2010, the latter are almost
392 systematically narrower than those of 2021 (compare the very narrow slides and flows in Fig. 5b with
393 the typically wider ones in Fig. 5a), while located in similar geological (limestone) and topographic
394 (hilly-mountainous) environments. Actually, in the so-called *Ravine du Sud* (Gorge of the South), part of
395 which is shown above in Fig. 3 (and in the annex, in Figs. A2 and A3), numerous very extensive slope
396 failures (but still relatively shallow) could be observed; most of them formed by coalescent neighboring
397 debris slides. Thus, entire slope units (delimited by upper and lateral slope crests and the valley bottom)
398 finally collapsed as one single mass movement. Such kind of extensive slope failures occurred far less
399 frequently in 2010 – at least onshore, while at least a few aforementioned coastal and mostly submarine
400 landslides must have been quite massive as their impact had triggered tsunami waves, as indicated above.
401 This assumption cannot be further verified as no higher resolution marine floor surface data are available.
402 However, we are aware that a full mapping of submarine or mixed subaerial-submarine slope failures

403 would be necessary to better understand the landslide distribution characteristics, especially for the 2010
404 event, as further discussed below.

405 The fact that no really massive landslides had occurred (onshore), both in 2010 and 2021, also explains
406 why only a few longer lasting landslide dams had formed on the rivers. We could identify only about 100
407 minor dams (with a volume of less than 50,000 m³, according to our estimate, based on the maximum
408 surface area value of about 5000 m² measured for the largest observed dam and a related maximum
409 possible thickness of 15 m, compared with the local morphological setting) after the August 2021 main
410 shock, most of which had disappeared before the end of October 2021; and, only a few dozens of them
411 were impounding temporary lakes. In this regard it should be noted that Martinez et al. (2021), who had
412 also mapped landslides triggered by the 2021 Nippes earthquake (4893, according to their open file
413 report), have outlined almost 300 (at least partial) landslide dams after the event. However, they also
414 indicate that most of them failed a few days after formation; still, at the time of publication of their open
415 file report in December 2021, they consider 35 of the remaining dams as potentially hazardous. Here, we
416 will not further analyze this aspect as any related hazard assessment would require a site-specific
417 approach that is not targeted by this first study completed at regional scale.

418



419

420 **Figure 5: a) GEPPro view (© Google Earth Pro) of landslides triggered by the August 2021 earthquake. b)**
 421 **GEPPro view of landslides induced by the January 2010 main shock (with landslide outlines by Harp et al.,**
 422 **2016).**

423

424 While debris slides are the predominant type of 2021 slope failures in the central mountain ranges,
 425 widespread soil slides (but of smaller volume, typically of less than 10,000 m³) had occurred along the
 426 hills (with an absolute crest altitude of less than 400 m, and a relative height of less than 200 m with
 427 respect to the nearby valley bottom) of the peninsula located in the southwest of Les Cayes (southern
 428 part of map in Fig. 4b). As the slopes are very gentle, often seem to be less than 5°, it could be that those
 429 failures, many of which affected agricultural areas (marked by brownish disrupted fields), are related to
 430 liquefaction phenomena. However, also this observation has to be reexamined, by ground-control and
 431 site-specific studies, as the remote analysis based on 1-m resolution imagery does not allow us to fully
 432 confirm this interpretation.

433 3.2 Landslide inventory and size-frequency statistics

434 3.2.1 Landslide inventory statistics

435 Table 1 presents an overview of general landslide inventory statistics, for both the 2010 and 2021 events.
436 The numbers in the first row show that apparently fewer landslides have been triggered in August 2021
437 (considering also the number of 4893 landslides published in the open file report by Martinez et al., 2021)
438 than in January 2010. At least two inventories, the one by Harp et al. (2016) and the one of Xu et al.
439 (2014), include far more landslide outlines (23,567 for the first, 30,828 for the second) than our catalogue
440 for 2021 (7091). Only the inventory by Gorum et al. (2013) that was the first one to be completed for the
441 2010 event contains fewer data (4490 points – not polygons - marking the landslide location). However,
442 paradoxically, a much wider surface area is covered by the apparently fewer 2021 landslides (a total area
443 of 84 km², see row 3 in Table 1) than by the more numerous 2010 landslides (sum of surface areas of
444 about 25 km², calculated for the Harp et al., 2016, inventory). This discrepancy will be discussed below,
445 considering the fact that 2021 landslides could only be mapped from higher resolution imagery for about
446 half of the potentially affected area (in the eastern part). For the western zone, only Sentinel-2 images
447 were available until the end of 2021. Those 10-m resolution images typically do not allow for the
448 (complete) mapping of landslides smaller than 2000 – 3000 m². Therefore, we focus only general
449 landslide inventory statistics, first, by comparing the observed landslide numbers with those predicted
450 by Havenith et al. (2016) and Malamud et al. (2014), respectively, for the two earthquakes – always
451 keeping in mind that the 2021 inventory is not complete for landslides smaller than about 3000 m² (this
452 value will also be analyzed below on the basis of the size-frequency relationship). As introduced above
453 (see Eq. 1), according to Havenith et al. (2016), this number depends on the seismic intensity (I, using
454 as input the I_a value computed for the respective earthquake magnitude), the fault factor (type, size and
455 possible surface rupture), the topographic energy (maximum difference of altitudes in the affected area),
456 the climatic background (in this case marked by tropical wet climate), and the lithological factor (here
457 using an average type, for rocks in general). For the precise classification of the different factors, the
458 reader is referred to Table 1 in Havenith et al. (2016). Here, we used the values presented below in Table
459 2 (considering both events in 2010 and 2021), which indicate the following:
460 1) the shaking intensity values, I=0.74, in 2010, and I=1 in 2021 are characteristic for the respective

461 magnitudes (note, this factor can reach a value of up to 3.5 in the case of high-magnitude earthquakes,
462 with $M_w > 8$);

463 2) the fault factor, $F=2.25$, can be considered as similar in both cases, marked by an oblique slip that
464 occurred along a fault segment with a length of 50-100 km, with no clear surface rupture (note, F can
465 reach a value of up to 6 in the case of a surface rupture of an activated reverse fault segment with a length
466 of more than 300 km, such as observed for the Wenchuan earthquake in 2008);

467 3) the topographic energy value, $TE=2$, in both cases characterizes a surface morphology marked by local
468 altitude changes of more than 500 m within a hilly region (only smaller mountains, with an altitude of
469 less than 2500 m can be found in the regions affected by the 2010 and 2021 events; note, Havenith et al.,
470 2016, selected a value 4 to mark the high steep slopes in the Longmenshan Mountains affected by the
471 Wenchuan earthquake in 2008);

472 4) the climatic background factor, $CB=1.5$ marks relatively wet conditions for the 2021 event while $CB=1$
473 indicates average conditions for the 2010 event (the higher value chosen for 2021 considers some
474 preconditioning of slope instability by Hurricane Matthew, as explained in the next section; note,
475 Havenith et al., 2016, selected a value $CB=2$ for the very wet conditions that can be found in the
476 Longmenshan Mountains affected by the Wenchuan earthquake, characterized by yearly precipitation
477 values of more than 3000 mm – while the target areas in Haiti are marked by values of about 2000 mm);

478 5) the lithological factor, $LF=2$, indicates that both weathered rocks and soft soils can be found in the
479 affected area (note, Havenith et al., 2016, selected a maximum value, $LF=4$, for the Haiyuan-Gansu-
480 Ningxia earthquake event, China, in 1920, as it affected an area that is almost entirely covered by Loess
481 deposits, which are highly susceptible to slope failure).

482 When these different factor values are combined according to Eq. (1) presented above, the total numbers
483 of landslides, N_{LT} , predicted for the 2010 and 2021 events are, respectively, 6694 and 13,476. These
484 values can be compared with the numbers predicted by the simple equation (Eq. 2), proposed by
485 Malamud et al. (2004), using only the earthquake magnitude as input: 2399 for the 2010 event and 4345
486 for the 2021 event. The latter prediction seems to clearly underestimate the observed numbers of
487 triggered landslides, while those predicted by using Eq. (1) by Havenith et al. (2016) provide intermediate
488 values: larger than the number observed by Gorum et al. (2013) but smaller than the numbers observed
489 by Harp et al. (2016) and by Xu et al. (2014). The two predictions (Eq. 1 and 2) were also applied to the

490 2021 event; the first one producing a higher N_{LT} (=13,476) than the observed value, the second one
491 producing a lower value (=4345).

492 As shown on the maps in Fig. 5, also the total area within the maximum extent of landslide occurrence,
493 $A_{L_{ext}}$, was outlined and then measured for the 2010 and 2021 events. Actually, related areas are relatively
494 similar: 4400 km² for 2021 and 4100 km² for 2010. These values can be compared in Table 1 with the
495 predictions by Havenith et al. (2016) and by Keefer and Wilson (1989), corresponding, respectively, to
496 3124 and 3467 km², for the 2010 event, and to 6470 and 5495 km², for the 2021 event. In this case, the
497 very simple equation proposed by Keefer and Wilson (1989) provides an estimate of $A_{L_{ext}}$ that is closer to
498 the observed value than the one produced by the more complex relationship proposed by Havenith et al.
499 (2016).

500 The third row of Table 1 compares the total observed slope areas affected by landslides, A_{LT} ,
501 corresponding, respectively, to a value of 24.86 km² for the 2010 event and of 84.38 km² for the 2021
502 event, with the values predicted by Eq. (5) by Malamud et al. (2004) for each event. For 2010, we applied
503 this relationship to the three observed values indicated in the first row and by using the N_{LT} , predicted
504 respectively by Havenith et al. (2016) and Malamud et al. (2004). Among all total landslide surface area
505 values predicted for the 2010 event, it can be seen that the one based on the Havenith et al. (2016) N_{LT}
506 estimate produces the best fit (=20.55 km²) when compared with the observed value of 24.86 km². For
507 2021, the respective predictions all underestimate the observed total landslide surface area value, A_{LT} , by
508 a factor of at least two, even when the highest N_{LT} estimate (using Eq. 1) by Havenith et al. (2016) is
509 used. Using the preceding information, it is also useful to compare the density values (here, expressed
510 in %) of landslide areas within the maximum extent surface area, which correspond to 0.5% and 2%,
511 respectively for the 2010 and 2021 events. Within the green rectangle (zone with highest landslide density)
512 shown in Fig; 4 above, even 20% of all the area is covered by landslides. Possible explanations for the
513 much larger total area (and the higher density) of landslides triggered in 2021 compared with 2010 will
514 be provided in the discussion.

515 The fourth and fifth rows show that the smallest landslide mapped by Harp et al. (2016) has a surface
516 area of 0.5 m² and their inventory contains 6587 landslide polygons smaller than 100 m² while our
517 inventory for 2021 only includes one landslide with a surface area smaller than this value. This
518 comparison also confirms that our inventory is likely to be incomplete for such small landslides, as there

519 is no physical reason why there would be much fewer smaller landslides triggered in 2021 than in 2010.
520 On the other hand, the largest landslide mapped for the 2021 event ($>400,000 \text{ m}^2$) has almost twice the
521 size of the largest one that occurred in 2010, when actually only 2 landslides larger than $100,000 \text{ m}^2$ had
522 been triggered; in 2021, we could outline more than 100 landslides larger than this value. And, for these
523 larger landslides we can be sure that we mapped them all and outlined them correctly, without
524 amalgamating distinct slope failures.

525 Finally, Table 1 provides information about the distribution of the 2010 and 2021 landslides with respect
526 to the blind fault rupture projected on the surface (near the EPGF outline). As already introduced above,
527 a much larger number of landslides occurred in the north of the latter in 2021 ($=4678$) compared to 2010
528 ($=2548$, at least for onshore slope failures); consequently, more landslides occurred in 2010 in the south
529 of the respective blind fault rupture. As the total number of mapped landslides is much larger for the
530 2010 event (which also means that only the relative proportions should really be considered), the
531 difference between those numbers is very high: 21,019 occurred in the south of the fault rupture in 2010
532 (about 90% of all landslides) and only 2420 in the south of the respective fault rupture in 2021 (about
533 35%). However, when the total surface area affected by landslides is considered, the 2021 event affected
534 more zones both in the south and the north of the fault rupture than the 2010 event, while the distribution
535 of landslides for each event with respect to the fault rupture remains the same also when considering the
536 affected surface areas: they are much larger in the south of the fault rupture for the 2010 event but larger
537 in the north for the 2021 event. The main explanation for this difference has already been provided above:
538 the fault segment that ruptured in 2010 is located close to the coast, with limited onshore surface areas
539 being exposed to landslide activity in the north of the respective fault rupture, while the location of the
540 fault rupture in 2021 is more central with respect to the shorelines of the southwestern peninsula of Haiti.

541

542

543

544

545

546 **Table 1: 2010 and 2021 landslide inventory characteristics – where not specified for the 2010 event, using the**
547 **Harp et al. (2016) inventory. The largest values for each specific observation/estimate (if more than 1 indicated)**
548 **are bold.**

Landslide inventory parameters/predictions	2010, Mw=7.0	2021, Mw=7.2
Observed number of landslides, N_{LT}	>4490 ^a / 23,567 ^b / 30,828^c	7091 /4893 ^d
Havenith et al. (2016) N_{LT} prediction 1	6694	13,476
Malamud et al. (2004) N_{LT} prediction 2	2399	4345
Area of region potentially affected by landslides, A_{Lext} (km ²)	4100	4400
Havenith et al. (2016) A_{Lext} prediction 1	3124	6470
Keefer and Wilson (1989) A_{Lext} prediction 2	3467	5495
Total surface area of landslides, A_{LT2} (km ²)	24.86	84.38
Malamud et al. (2004) A_{LT} prediction :		
for the observed N_{LT}	13.8 ^a / 72.3 ^b / 94.6^c	21.8
for the N_{LT} prediction 1	20.55	41.4
for the N_{LT} prediction 2	7.36	13.3
Smallest landslide (m ²)	0.5	75
Number of landslides smaller than 100 m ²	6587	1
Largest landslide (m ²)	234,370	409,479
Number of landslides larger than 100,000 m ²	2	103
Total number of landslides in the north (N) / south (S) of the fault rupture	N= 2548 S= 21,019	N= 4678 S= 2420
Total surface area of landslides in the N / S of the fault rupture (km ²)	N= 2.45 S= 22.41	N= 58.31 S= 26.07

549 ^a Number of landslides observed by Gorum et al. (2013), ^b by Harp et al. (2016), ^c by Xu et al. (2014),
550 and ^d by Martinez et al. (2021).

551

552 In addition to the numbers shown in Table 1 and explained above, we also provide two values for the
553 smaller landslide inventory compiled for the period between October 10, 2016 and the end of 2017. For
554 this period, 625 landslide zones have been outlined (see yellow polygons shown on the views and map
555 in Figs. 3 and 4), covering a total surface area of 9.5 km² (located within an area of maximum extent of
556 these landslides of 1770 km² as outlined in yellow, above in Fig. 4) This also means that about 0.5% of
557 the area within the maximum extent was covered by landslides. Highest concentration of landslides can

558 be observed within the green rectangle shown in Fig. 4, where 3% of the total area is covered by
 559 landslides. However, we must indicate that these values represent approximations as only 50% of the
 560 potentially affected area is covered by cloud-free imagery on GEPPro for this period, most of which
 561 actually covers the short period between October 10 and 28, 2016 (just after Hurricane Matthew event).
 562 Post-2017 imagery was not used as we could observe that many landslides identified shortly after Oct.
 563 10, 2016, had already ‘disappeared’ in 2018-2020 due to revegetation of the affected area (see, above,
 564 the comparison between GEPPro views of October 2016 and February 2020 in Fig. 3).

565 **Table 2: Factors contributing to the total number and surface area of landslides triggered by the 2010 and the**
 566 **2021 earthquakes, according to the prediction proposed by Havenith et al. (2016). The minimum and**
 567 **maximum values proposed by Havenith et al. (2016) are also indicated, the latter with information on the**
 568 **event – region, to which this maximum factor value was attributed.**

Haiti Events/ Factors	Shaking Intensity, I	Fault Factor, F (type, FT)	Topographic Energy, TE	Climatic Background, CB	Lithological Factor, LF	Hypocentral Depth, D (km)
2010	0.74	2.25(1.5)	2	1.5	2	10
2021	1	2.25(1.5)	2	1	2	10
min. values	0.1	0.75	1	0.5	1	10
max. values (event - region)	3.4 (Chile, 1960)	6 (Wenchuan, 2008)	4 (Wenchuan, 2008)	2 (Wenchuan, 2008)	4 (Haiyuan-Gansu- Ningxia, 1920)	226 (Hindu Kush, 2002)

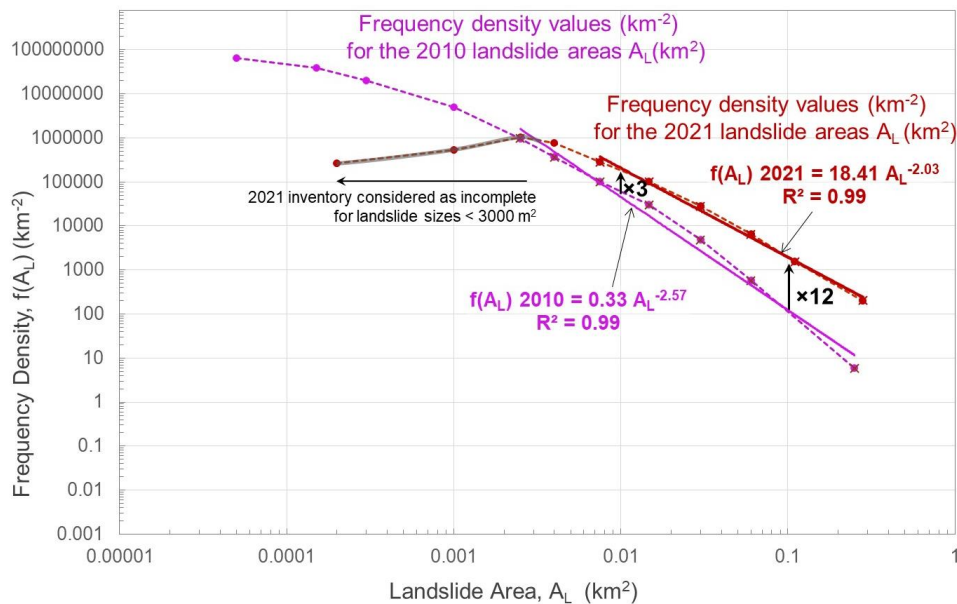
569

570 3.2.2 Landslide size-frequency statistics

571 We also computed frequency-density values for various landslide surface area classes as shown on the
 572 graph in Fig. 6. There are two important parameters to be analyzed for the observed frequency-density
 573 distributions, according to Malamud et al. (2004), among others: the first part is represented by the
 574 power-law decay (see also introduction in Stark and Hovius, 2001) that appears as a linear decay in the
 575 log-log graph below; the second part is the so-called ‘rollover’, which can be observed for a landslide
 576 surface area where the exponentially decreasing number of larger landslides turns into a decrease of the
 577 number of smaller landslides. Here, we will only focus on the power-law decay that can be observed for
 578 the larger landslides, for which we consider both, the 2010 and the 2021, inventories as complete. Fig. 6
 579 shows that such a power-law decay can be observed for 2010 landslides larger than 2000 m² and for 2021

580 landslides larger than about 4000 m². This comparison confirms the likely incompleteness of the 2021
 581 inventory, even for landslides smaller than 4000 m². The rollover part will not be analyzed here as it
 582 occurs for smaller landslides, well below this limit of completeness of our 2021 inventory (referring to
 583 estimates by Malamud et al., 2004).

584 For the larger landslides, the comparison between frequency density outputs of the 2010 and 2021
 585 landslide inventories presented in Fig. 6 first shows that related values are higher for the latter catalogue.
 586 Actually, related frequency density values are three times larger for the landslide size class of 10,000 m²
 587 and even twelve times for the one of 100,000 m². And, for those larger landslide classes, the absolute
 588 value of the power-law decay is slightly higher (-2.57, for the pink line fitting the 2010 data) for the 2010
 589 inventory than for the 2021 one (-2.03, for the red line fitting the 2021 data). Thus, the relative smaller
 590 decay exponent observed for the 2021 landslide inventory explains why related frequency density values
 591 are increasingly (i.e. for larger landslide sizes) higher compared with the 2010 values observed for the
 592 same landslide size classes. These different size-frequency characteristics of the 2010 and 2021
 593 landslides inventories will shortly be discussed below (considering the constraint of inventory
 594 completeness for both events), but the most important information to be retained at this level is that for
 595 all landslide classes larger than 4000 m² more landslides have been observed in 2021 than in 2010.



596

597 **Figure 6: Frequency density graphs developed for the 2010 (in pink, by Harp et al., 2016) and the new 2021**

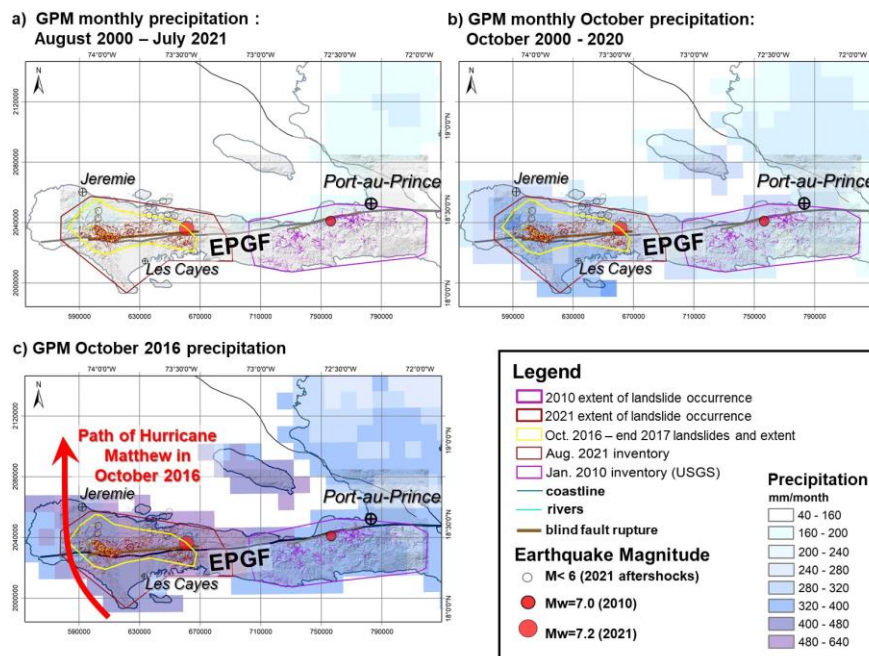
598 **landslide inventories (in dark red), with related power-law decays outlined.**

599 3.3 Climatic (pre- and post-seismic) conditioning of slope instability

600 The climatic influence on landslide occurrence (in 2021) has been introduced above, by considering the
601 possible impacts of hurricanes on slope failure occurrence, marked both by preconditioning of slope
602 instability and by post-seismic intensification. We first start analyzing the last effect, by considering the
603 potential impact of Hurricane Grace on post-seismic landslide intensification, on August 16-17, 2021
604 (when it had crossed the target region and was actually classified as tropical depression at that stage). A
605 possible effect of related rainfalls on landslide occurrence has already been highlighted, for instance, on
606 the AGU Landslide blog (by Petley, D., 2021, on blogs.agu.org/landslideblog). This effect could be
607 confirmed when we compared Sentinel-2 imagery collected right after the earthquake (2h after the main
608 shock) with images remotely sensed after August 17, 2021. As indicated above and shown in Fig. 4, an
609 intensification of denudation could indeed be observed after the tropical storm Grace event. However,
610 one important limitation has to be highlighted: this comparison could only be completed for about 10%
611 of the area potentially hit both by the earthquake and by Grace, due to the intense cloud cover present in
612 the target region during that period. Furthermore, another effect could have contributed to slope failure
613 intensification after the main shock on August 14, the one related to the aftershocks (see empty circles
614 shown in all maps above), but analyzing this effect would require a refinement of the satellite image
615 analysis both in space and time, which is hardly possible considering the extensive cloud cover present
616 in the target area when all those seismic shocks occurred. Here, we will focus on the possible climatic
617 influence, which can better be outlined when comparing the landslide distribution with actual
618 precipitation maps. Therefore, we used the aforementioned Global Precipitation Measurement Mission
619 (GPM) data. Fig. 7 presents the three following types of GPM maps: average monthly precipitation maps
620 for the whole period of 2000 – July 2021, for all months of October between 2000-2020, and for October
621 2016, when Hurricane Matthew had crossed the island.

622 While comparing the average monthly precipitation rates between 2000 and 2021 (Fig. 7a) with the one
623 of October 2016 (Fig. 7c) we can see that, for the latter month, a peak of intensity of 626 mm can be
624 observed for the area between Gran Rivière De Nappe and Petite-Rivière-de-Nippes, situated
625 immediately in the north of the epicentral area of the 2021 main shock. Actually, the whole area
626 potentially affected by the August 2021 earthquake had been exposed to clearly higher precipitation rates

627 of more than 400 mm in October 2016, while, according to the GPM, average precipitation recorded in
 628 October between 2000 and 2020 varies typically between 200 and 320 mm (as shown by the map, in Fig.
 629 8b). For October 2016, those values were also the highest ones compared with the rest of the country;
 630 this clearly indicates that they must be related to a specific climatic event, which can easily be identified
 631 as Hurricane Matthew that had crossed the western peninsula (including the region hit later by the August
 632 2021 earthquake) on October 4-5, 2016. And, precisely for this region that had been exposed to abnormal
 633 precipitation rates in October 2016, we could outline 625 landslides triggered after the Hurricane
 634 Matthew event, and before the end of 2017 (yellow polygons shown above in the maps in Figs 1, 2, 3
 635 and 4 and below in Fig. 7). And, most of these October 2016 – end of 2017 landslide zones (at least 90%
 636 of them) are located within those mapped for the August 2021 seismic event (which are still marked by
 637 a much higher level of denudation compared to the October 2016 activation). In the discussion, we will
 638 analyze how such Hurricane Matthew might have preconditioned slope instability in the region hit by
 639 the August 14, 2021, earthquake. We will also consider a general influence of tropical storms on the wide
 640 distribution of the landslides triggered in 2010 (and also for those triggered in 2021, in addition to the
 641 Hurricane Matthew effect).



642
 643 **Figure 7: Monthly © Global Precipitation Measurement Mission (NASA) maps (0.1° resolution, values in**
 644 **mm/month) for southwestern Haiti, (a) for all months between August 2000 and July 2021, (b) for the month**
 645 **of October between 2000 and 2020, and (c) for October 2016 (marked by the Hurricane Matthew event).**

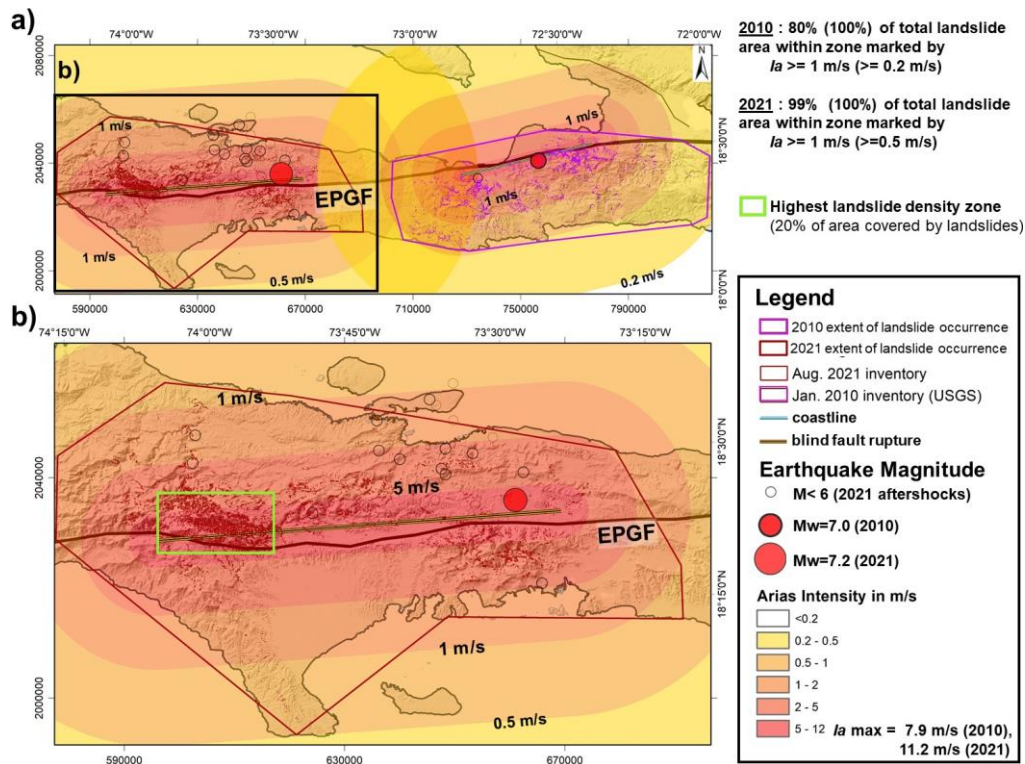
646 By comparing equivalent data (not shown here) of the merged satellite-gauge precipitation estimate for
647 August 2021 with the monthly precipitation map averaged for all months of the previous 20 years, we
648 can clearly see that August 2021 was indeed marked by a higher precipitation rate, which is most likely
649 related to the Grace event. However, the most intense precipitation did not affect the region hit by the
650 2021 earthquake but the eastern part of the peninsula, roughly covering the same region as the one
651 affected by the 2010 event (note, we did not check any landslide reactivation after Grace for that area).
652 The region hit by the 2021 earthquake was not affected by much higher monthly precipitation rates than
653 usual: for the central seismically affected zone, in the north of Les Cayes, about 240-280 mm had been
654 recorded in August 2021, against a monthly average of 200 mm. Thus, just by considering these data,
655 one would not expect an important climatic contribution to slope failure occurrence in the region affected
656 by the 2021 earthquake. Still, an influence could be observed and this is likely to be related to the
657 concentration of most of the ‘monthly precipitation’ of August 2021 within the two days (Aug. 16 and
658 17) of the Grace tropical storm event, just two days after the 2021 main shock. As indicated above, we
659 estimate that related precipitation has resulted in an increase of landslide surface areas of about 10-15%.
660 Due to the limited extent of zones where this check can be made (only considering the cloud-free areas
661 on the Sentinel-2 image of August 14, 2021), it was decided to map all areas covered by landslides after
662 August 14, 2021, also those which are likely to have been (re)activated by rainfall – the total effect of
663 which can barely be controlled and quantified outside the 10% of cloud-free zones visible on the image
664 collected right after the main shock. The only ‘correction’ that can be made is to reduce the total surface
665 area mapped as landslides by those 10-15% to estimate the one that was actually affected by co-seismic
666 slope failures: thus, instead of considering the value of 84 km², it is possible that co-seismic landslides
667 covered a total surface area of ‘only’ 75-78 km² – which is still three times more than the total surface
668 area covered by 2010 co-seismic landslides (close to 25 km²).

669

670 **3.4 Shaking intensity maps**

671 Above, we first analyzed the possible climatic influence on seismically induced slope failures as it could
672 affect the landslide distribution and thus has to be taken into consideration when assessing and
673 interpreting the seismic effect on landslide occurrence. The latter will only be analyzed here at regional

674 scale. Therefore, we compare the landslide distributions observed for the 2010 and 2021 events with the
675 respective estimated Arias Intensity (I_a) attenuation maps, computed by applying Eq. (7b) introduced
676 above, as recommended by Wilson and Keefer (1985) and also by later studies (e.g., Harp and Wilson,
677 1995, among many others). The map in Fig. 8a presents the 2010 and 2021 mainshock I_a attenuation
678 values, with a maximum shaking intensity of 11.2 m/s computed for the 2021 event and 7.9 m/s for 2010
679 (respective maps are partly overlapping in the central region, but not summed up, keeping the individual
680 values). This map shows that all 2010 and 2021 landslides are included within a zone marked by an I_a
681 threshold of 0.2 m/s (close to the one proposed by Keefer and Wilson, 1989, for disrupted slides and
682 falls). Actually, for 2021, 99% of the total landslide surface areas are even located within a zone marked
683 by I_a values larger than 1 m/s; however, only 80% of the total surface areas of the 2010 landslides are
684 included within the respective $I_a \geq 1$ m/s zone. Thus, the latter mass movements appear as more
685 ‘dispersed’ with respect to the estimated seismic intensity attenuation than the 2021 ones. The latter are
686 most concentrated, as indicated above, within the green rectangle (see Fig. 8b, marked by I_a values of 4-
687 11 m/s) with an area of 200 km² that contains 40 km² of landslide-covered zones (=20% of total area).
688 Notwithstanding the relative dispersion of 2010 landslides, and the overlap of I_a values larger than 0.2
689 m/s in the central zone between the two blind fault ruptures of 2010 and 2021, not a single landslide of
690 2010 seems to have been reactivated in 2021. This observation raises the question if the central ‘landslide
691 gap’ is due to an overestimation of the I_a values in this central zone (as this zone is marked by I_a values
692 above the aforementioned minimum threshold of 0.2 m/s, for both events, and thus should have been
693 affected by landslides both in 2010 and 2021, according to the shaking intensity prediction parameter),
694 or if this zone is simply less susceptible to (seismic) slope failures.



695

696 **Figure 8: a) Arias Intensity (I_a) attenuation maps computed (by using Eq. 7b, by Keefer and Wilson, 1989)**
 697 **for the 2010 and 2021 main shocks in Haiti; see also indication of % of total surface area of landslides observed**
 698 **for different I_a thresholds. b) Focus on the respective map computed for the 2021 event.**

699

700 To answer this and other related questions, a full landslide susceptibility analysis has been completed
 701 and will be presented in another paper. Here, only the possible links between landslide distribution the
 702 aforementioned seismotectonic and climatic factors will be discussed.

703 4 Discussion

704 4.1 Discussion about landslide distribution characteristics

705 From the comparison of the two landslide catalogues (2010 and 2021), we could first infer that apparently
 706 not a single landslide triggered in August 2021 occurred within the zone previously impacted by the 2010
 707 event. There is a gap of about 10 km between the westernmost 2010 and the easternmost 2021 landslide
 708 (see gap between the general outlines of the maximum extent of landslides triggered in 2010 and in 2021

709 shown on the map in Fig. 4a). Thus, we assume that there was no obvious preconditioning of landslide
710 generation in 2021 by the 2010 event, while landslide studies completed in other parts of the World (e.g.,
711 by Parker et al., 2015, for events in New Zealand) could outline an influence of previous earthquakes on
712 landslide occurrence during later events. The absence of this influence by the 2010 earthquake is
713 probably due to the long distance (the ‘gap’) of about 60 km between the fault segments that ruptured in
714 2010 and in 2021. However, by citing Saint Fleur et al. (2020), Stein et al. (2021) hint at an older event,
715 of 1770, with an assumed magnitude of 7.5 and an epicenter located precisely in the gap between the
716 2010 and 2021 blind fault ruptures, which could also have affected the region hit by the 2021 earthquake.
717 At present, we cannot exclude that this older event had preconditioned some slopes (by soil weakening,
718 rock fracturing) affected by some larger landslides in 2021; however, very shallow slope failures initiated
719 in 1770 are unlikely to have stayed in place over such a long period of more than 250 years, as they
720 would have been ‘washed’ away by the next tropical rains.

721 Second, none of the two earthquakes triggered very massive landslides, such as deep-seated rockslides
722 with a volume of more than 10^{10} m^3 (while extensive areas are covered by layered and weathered
723 limestone that could also produce massive slope failures; but this aspect will not be further discussed
724 here as the related geological influence on landslide occurrence will be analyzed in the landslide
725 susceptibility paper presently under preparation). Such massive failures have been observed after many
726 M7+ events in other mountainous regions of the world: see Fan et al. (2018) for the 2008 Mw=7.9
727 earthquake in China, or Havenith et al. (2015) for a series of M>7 events that hit Central Asian mountain
728 regions during the last 120 years. This is partly due to the fact that the regions hit by the two earthquakes
729 in Haiti are represented by mountains of limited elevation changes, typically less than 1000 m – while,
730 for instance, the Longmenshan Mountains hit by the 2008 Wenchuan earthquake, present elevation
731 changes of up to 3000 m over relatively short (<6 km) distances (Fan et al., 2018). This fact, combined
732 with the higher magnitude of the Wenchuan earthquake (Mw=7.9), could partly explain the much larger
733 number of massive rockslides triggered by the latter event in China. However, we have also to consider
734 some counterexamples of regions marked by mountainous relief that did not produce any very massive
735 rockslides during high-magnitude earthquakes (just like the 2010 and 2021 Haiti events), such as the part
736 of the Himalayas hit in 2015 by the Gorkha earthquake (see Lacroix, 2016). Thus, this problem related
737 to the more or less likely occurrence of massive rockslides in regions hit by high-magnitude earthquakes

738 is relatively complex, and cannot purely be approached by spatial analysis, as the one presented here;
739 more extensive numerical simulations would actually be necessary (but are definitely not the target of
740 our studies in Haiti) to assess the potential of seismically induced rockslides, such as those presented in
741 Gischig et al. (2015) or Lemaire et al. (2021).

742 Third, considering the values presented in Table 1, we still have to explain why the total surface area
743 covered by landslides in 2021 is much larger than the one covered by the 2010 landslides. We estimate
744 that this fact is likely to be related to (a combination of some of) the four following points: a) the first
745 likely physical reason for the larger area hit by mass movements in 2021 is the higher triggering
746 earthquake magnitude of the last event (this effect is also analyzed by comparing the influence of shaking
747 intensity on landslide distribution); b) another physical reason could be the possibly higher susceptibility
748 to mass movements of the western part of the peninsula hit by the 2021 event, compared to the eastern
749 part (this factor has to be analyzed on the basis of landslide susceptibility maps, considering also the
750 geological influence, which have been computed and will be presented in a follow-up paper); c) a third
751 reason for the larger area affected by landslides in 2021 could be related to the aforementioned ‘hurricane’
752 effects that will be further discussed below; d) and fourth, the more central location of the fault segment
753 activated in 2021 with respect to the coasts of the peninsula certainly also explains parts of the larger
754 total surface areas of (subaerial) slope failures triggered during the last event within the wider onshore
755 hanging wall part, as already introduced above.

756 In this regard, we also highlighted the fact that the 2010 event triggered most landslides in the south of
757 the activated fault segment, while in August 2021 about 2/3 of all landslides were triggered in the north
758 of it. Considering the oblique slip character along the fault ruptures of 2010 and 2021 dipping to the
759 north, the hanging wall is located on the northside of the blind fault rupture projected on the surface -
760 (according to the fault mechanism provided by the USGS Earthquake Hazard Program page,
761 earthquake.usgs.gov). In this regard, the Wenchuan earthquake has clearly marked the effect of the
762 hanging wall on the landslide distribution: about 90 % of all landslides were triggered on top of the
763 reverse fault dipping towards the west-northwest, only a minor portion occurred on the more ‘stable’ foot
764 wall (Gorum et al., 2011; Fan et al., 2018). The ‘hanging wall effect’ on landslide triggering can be
765 explained by stronger upward oriented shaking that contributes to a higher surface acceleration and more
766 intense slope failures; additionally, all (or most of the) aftershocks occurred within the hanging wall,

767 increasing the seismic shaking intensity cumulated over the active seismic period in the related surface
768 area, which could have contributed to prolonged landslide activity as well (to be added to the climatic
769 effect introduced above and discussed below). This effect may thus also be at the origin of the more
770 widespread landslide occurrence in the north of the 2021 blind fault rupture. The reduced number of
771 ‘subaerial’ landslides induced on the hanging wall side of the 2010 fault rupture can be explained by the
772 relative proximity of the respective fault rupture to the coast in the north and the absence of high and
773 steep slopes (onshore) on this side. Actually, a few known massive landslides occurred near the coast,
774 but are mostly located on submarine slopes in the 2010 hanging wall zone. Three of them reportedly also
775 caused tsunami waves (see Olson et al., 2011, among others) – a phenomenon that was not observed for
776 the 2021 event, as the coasts are located farther away from the seismic source zone.

777 **4.2 Discussion about landslide size-frequency characteristics**

778 Above, we clearly outlined the incompleteness of our 2021 inventory, for landslides smaller than about
779 3000 m²; thus, it is likely that thousands of smaller landslides could not be mapped from the medium-
780 resolution Sentinel-2 imagery (10 m) and the higher resolution imagery (0.5 – 1 m) available on GEPro
781 for 50% of the target area before the end of 2021. To refine our landslide mapping in future, higher
782 resolution imagery must be used for the whole area affected by the 2021 event, and automatic landslide
783 identification techniques shall be applied by combining image analysis and machine learning as proposed
784 by Amatya et al. (2021). Actually, the ‘manual’ mapping applied now would take too much time to outline
785 the many thousands of very small landslides that have not been identified so far. Those would contribute
786 to the increase of the weight of the smaller landslides in the 2021 inventory, especially of those smaller
787 than 3000 m².

788 The incompleteness of the inventory notably limits its use for size-frequency analyses. However, above
789 we still presented related statistics and compared them with those made for the 2010 landslide inventory
790 to point out the clearly higher numbers of larger landslides triggered by the last event, compared with the
791 one in 2010 (based on ‘landslide size’ classes, for which the 2021 inventory can be considered as
792 complete). Actually, landslides triggered in 2010 mainly consisted of narrow slides and flows in
793 weathered limestone rocks, while the 2021 earthquake also induced landslide processes over wider slope
794 areas – as clearly shown by the 2021 and 2010 landslide zone views presented in Fig. 5; in the *Ravine*

795 *du Sud*, even entire slope units had failed in August 2021 (but the failed parts were typically not very
796 thick, less than 10 m).

797 **4.3 Discussion about climatic pre-conditioning effects**

798 We estimate that the different climatic conditions observed before the respective events may partly
799 explain the more widespread occurrence of larger landslides related to the 2021 event. In this regard we
800 indicated that the climatic contribution to landslide activity in 2021 might be twofold: first, some post-
801 seismic intensification of slope failures could be observed after the tropical storm Grace event that had
802 crossed the earthquake region on August 16-17, two days after the main shock. However, related effects
803 cannot really be quantified as only 10% of the total surface area potentially affected by the earthquake
804 appeared as cloud-free on imagery available right after the August 14 main shock and before August 16
805 (Grace event). For those limited areas, we estimate that storm Grace caused a widening of about 10-15%
806 of all slope failures with respect to the purely earthquake-induced landslide activation. Second, by
807 comparing the 2016-2017 landslide distribution with the one observed after August 14, 2021, it can be
808 seen that most of the October 2016 – end 2017 landslides occurred within the same region as the 2021
809 ones and most were clearly reactivated by the seismic shaking in August 2021 (while also many of them
810 had been revegetated in between). Above we could show that Hurricane Matthew had crossed the western
811 part of the peninsula in October 2016, producing an abnormal amount of precipitation precisely over the
812 area that was later hit by the earthquake (see GPM maps in Fig. 7), and where also hundreds of landslides
813 had occurred just after mid-October 2016. Therefore, it is very likely that this climatic event has triggered
814 many (and probably most) of the 625 mapped pre-seismic (October 2016 - pre-2018) landslides, which
815 preconditioned slope instability all over the area hit by the 2021 earthquake. Preconditioning of the
816 August 2021 slope failures could have been related to rock weakening and fracturing, and removal of the
817 protective vegetation cover during the 2016 Matthew event. Indeed, practically all 625 mapped October
818 2016 – pre-2018 landslide zones (at least 90% of them – and, considering that only for 50% of the entire
819 potentially affected area in 2016 landslide could be mapped over cloud-free zones) are located within the
820 landslide areas mapped for the August 2021 seismic event (which are still marked by a much higher level
821 of denudation compared to the October 2016 activation). The double hurricane effect (by Matthew in
822 2016 and by Grace just after the 2021 main shock) observed in the area hit by 2021 earthquake could be

823 responsible for the proportionally larger size of the 2021 landslides (estimating that the 2016 event, due
824 to its extreme intensity, made the strongest contribution) compared with the 2010 ones. In addition, we
825 have to consider that the 2010 earthquake had not been preceded by any particular hurricane event during
826 the previous ten years, at least not by any storm that had caused abnormal precipitation amounts (similar
827 to those caused by Hurricane Matthew) within the region hit by the 2010 earthquake.

828 Furthermore, the combined seismic and climatic influence could also explain the very different spatial
829 landslide distribution characteristics of the 2010 and 2021 catalogues: the relative dispersion of
830 landslides observed after the 2010 event could thus be partly related to the spatially highly variable effect
831 of tropical storms and hurricanes on landslide activity (acting over a longer period, with an influence that
832 could last over tens of years), partly overprinting the more concentrated seismic effect (resulting in
833 clusters of mass movements near the seismic source zone). The same dispersion might also have been
834 observed for the 2021 event if the central part of the seismically affected area had not been hit by that
835 major climatic event just five years before – doubling the landslide concentration effect in that area
836 (specifically for the 2021 event). However, we acknowledge that a quantification of these opposite effects
837 of climatic events, both on landslide dispersion and on their concentration, requires a more detailed
838 analysis, also focusing on specific sites, by completing numerical simulations of mass movements
839 affected by variable climatic (modelling changing groundwater level) and seismic influences (including
840 the effect of rock structures and types of lithologies and morphologies on shaking polarization and
841 amplification). A related landslide spatial distribution analysis should then also consider the influence of
842 extensive deforestation on slope destabilization, all over the country of Haiti. Actually, deforestation is
843 responsible for the decrease of 90% of the primary forest over the last few tens of years, especially in the
844 southern regions of Haiti where the two earthquake events had occurred (see Hedges et al., 2018). As
845 mostly shallow landslides occurred in 2010 and 2021, the effect of deforestation on the destabilization
846 of shallow soils and weathered rock cover must be taken into consideration for landslide occurrence
847 prediction. Such an extensive study would thus require the creation of an integrated seismotectonic-
848 morpho-geological-climatic-soil cover model allowing us to fully understand changing landslide activity
849 in Haiti – which is not the target of the present analysis (but will be partly approached in the follow-up
850 paper).

851 **4.4 Discussion about the regional seismic shaking influence on landslide distribution**

852 As for the climatic part, here, we only present regional data to outline some general seismic influences
853 on landslide activity induced by the 2010 and 2021 earthquakes. Related maps (Fig. 8) show that the
854 aforementioned gap of landslides between the areas affected by the earthquakes in 2010 and 2021 would
855 indeed be marked both by a lower shaking intensity (but showing values that are still larger than the
856 threshold Ia values observed elsewhere for landslide occurrence) and lower landslide susceptibility (a
857 result that still has to be published). In the annex (Fig. A1), we also present the shakemaps produced by
858 the USGS for the two events, but we did not compare landslide distributions with these maps as the latter
859 do not seem to be coherent with respect to each other, noting that much larger intensities would have
860 been produced by the lower magnitude event of 2010. Actually, it should be considered that such maps
861 are also influenced by regional site effects (mostly on flat areas) that are not really relevant for landslide
862 trigger mechanisms, and are also depending on ground measurements of seismic intensity that had not
863 been well constrained during the 2010 due to missing seismic stations in Haiti at that time (a problem
864 that starts to be solved now).

865 **5 Conclusions**

866 In this paper we presented a new landslide inventory created for the $M_w=7.2$ Nippes earthquake that
867 occurred on August 14, 2021, in Haiti. Related spatial and statistical characteristics have been compared
868 with those of the landslides mapped by others for the previous, $M_w=7.0$, January 12 (2010), earthquake
869 that had occurred along the same fault zone (EPGF zone) but more to the East. Considering a series of
870 uncertainties affecting the landslide statistics (related to the mapping technique, including the uncertain
871 number of particularly small landslides triggered in 2021) and the environmental information (including
872 some general climatic and geological conditions), this comparison allowed us to highlight the following
873 points: 1) the 2021 earthquake triggered clearly bigger landslides than the one in 2010, and also the sum
874 of all landslide areas is much larger than the one computed for the 2010 event; 2) a climatic
875 preconditioning of slope instability could be outlined for the 2021 event, mainly in connection with the
876 impacts of recent hurricanes in the 2021 affected region, which could also partly explain the more
877 extensive landslide activity observed in 2021; 3) the 2010 landslides seem to be more dispersed around

878 the epicentral area than the 2021 slope failures, which could be due to the opposite climatic effect
879 inducing spatially more variable slope destabilization (also as no particular storm had hit the 2010
880 affected region just before or after the seismic event, as it was the case in 2021); this dispersion effect
881 can also be enhanced by the spatially varying deforestation that is locally very intense in the target areas.
882 We estimate that this proof of a likely combined seismic and climatic influence on landslide activity
883 (possibly augmented by morpho-geological and soil cover effects not studied in detail here) opens new
884 avenues for geohazard research, especially for regions like Haiti that are regularly hit both by severe
885 earthquakes and weather events. We also think that preconditioning of slope failures by multiple events
886 over longer terms, including by former earthquakes, should be studied more in detail as this
887 preconditioning could highly contribute to local and regional landslide hazards, both over short and
888 longer terms. A full analysis of such a scenario would require the development of an integrated
889 seismotectonic-morpho-geological-climatic-soil (and vegetation) cover model, combing extensive
890 spatial analyses with detailed numerical simulations, which can only be completed through an extensive
891 international multi-disciplinary collaboration around this target – which is obviously missing for Haiti.
892 Assessment of related risk would further require the involvement of experts in social geography and
893 economy. Also, a closer collaboration between scientists and the population shall be promoted as
894 recommended by Calais et al. (2022) and von Hillebrandt-Andrade and Vanacore (2022). Only when
895 these goals are achieved, we could really work on the prevention of at least parts of another future
896 earthquake disaster in Haiti.

897

898 **Acknowledgments**

899 This study was partly supported by the ‘Earthquake Hazard and Vulnerability assessment – developing
900 innovative solutions for sustainable Risk Reduction and Communication in Haiti’ project funding (2019-
901 2024) provided by the Belgian ARES – ACADÉMIE DE RECHERCHE ET D’ENSEIGNEMENT
902 SUPÉRIEUR.

903

904 **References**

905

906 Acker, G., and Leptoukh, G.: Online Analysis Enhances Use of NASA Earth Science Data, *Eos, Trans.*
907 *AGU*, 88(2), 14–17, 2007.

908 Amatya, P., Kirschbaum, D., Stanley, T., and Tanyas, H.: Landslide mapping using object-based image
909 analysis and open source tools, *Eng. Geol.*, 282, 10 p., doi:10.1016/j.enggeo.2021.106000, 2021.

910 Arias, A.: A measure of earthquake intensity, In *Seismic design for Nuclear Powerplants*, R.J. Hansen
911 (ed), MIT Press, Cambridge, Massachusetts, 438–483, 1970.

912 Calais, E., Freed, A., Mattioli, G., Amelung, F., Jónsson, S., Jansma, P., Hong, S. H., Dixon, T., Prépetit,
913 C., and Momplaisir, R.: Transpressional rupture of an unmapped fault during the 2010 Haiti
914 earthquake, *Nature Geoscience*, 3(11), 794–799, doi:10.1038/ngeo992, 2010.

915 Calais, E., Symithe, S., Monfret, T., Delouis, B., Lomax, A., Courboux, F., Ampuero, J.P., Lara, P.E.,
916 Bletery, Q., Chèze, J., Peix, F., Deschamps, A., de Lépinay, B., Rimbault, B., Jolivet, R., Paul, S., St
917 Fleur, S., Boisson, D., Fukushima, Y., Duputel, Z., Xu, L., and Meng, L.: Citizen seismology helps
918 decipher the 2021 Haiti earthquake, *Science*, 376 (6590), 283–287, doi:10.1126/science.abn1045,
919 2022.

920 Fan, X., Juang, C.H., Wasowski, J., Huang, R., Xu, Q., Scaringi, G., van Westen, C.J., and Havenith,
921 H.B.: What we have learned from the 2008 Wenchuan Earthquake and its aftermath: A decade of research
922 and challenges, *Eng. Geol.*, 241, 25–32, doi:10.1016/j.enggeo.2018.05.004, 2018.

923 Frankel, A., Harmsen, S., Mueller, C., Calais, E., and Haase, J.: Seismic hazard maps for Haiti.
924 *Earthquake Spectra*, 27(SUPPL. 1), 23–41, doi:10.1193/1.3631016, 2011.

925 Fritz, H. M., Hillaire, J. V., Molière, E., Wei, Y., and Mohammed, F.: Twin tsunamis triggered by the 12
926 January 2010 Haiti earthquake, *Pure and Applied Geophysics*, 170(9), 1463–1474, doi:10.1007/S00024-
927 012-0479-3, 2013.

928 Gischig, V., Eberhardt, E., Moore, J., and Hungr, O.: On the seismic response of deep-seated rock slope
929 instabilities — insights from numerical modeling. *Eng. Geol.*, 193, 1–18, doi:
930 10.1016/j.enggeo.2015.04.003, 2015.

931 Gorum, T., Fan, X., van Westen, C.J., Huang, R., Xu, Q., Tang, C., and Wang, G.: Distribution pattern
932 of earthquake-induced landslides triggered by the 12 May 2008 Wenchuan earthquake, *Geomorph.*,
933 133(3–4), 152–167, doi:10.1016/j.geomorph.2010.12.030, 2011.

934 Gorum, T., van Westen, C.J., Korup, O., van der Meijde, M., Fan, X., and van der Meer, F.D.: Complex
935 rupture mechanism and topography control symmetry of mass - wasting pattern, 2010 Haiti earthquake,
936 *Geomorph.*, 184, 127–138, doi:10.1016/j.geomorph.2012.11.027, 2013.

937 Harp, E.L., and Wilson, R.C.: Shaking intensity thresholds for rock falls and slides: evidence from 1987
938 Whittier Narrows and Superstition Hills earthquake strong-motion records, *Bull. Seis. Soc. Am.*, 85,
939 1739–1757, 1995.

940 Harp, E.L., Jibson, R.W., and Schmitt, R.G.: Map of landslides triggered by the January 12, 2010, Haiti
941 earthquake: U.S. Geological Survey Scientific Investigations Map 3353, 15 p., 1 sheet, scale 1:150,000.
942 doi:10.3133/sim3353, 2016.

943 Havenith, H.B., Strom, A., Torgoev, I., Torgoev, A., Lamair, L., Ischuk, A., and Abdrakhmatov, K.: Tien
944 Shan Geohazards Database: Earthquakes and Landslides, *Geomorph.*, 249, 16–31,
945 doi:10.1016/j.geomorph.2015.01.037, 2015.

946 Havenith, H.B., Torgoev, A., Braun, A., Schlögel, R., and Micu, M.: A new classification of earthquake-
947 induced landslide event sizes based on seismotectonic, topographic, climatic and geologic factors,
948 *Geoenviron. Disasters*, 3(6), 2–24, doi:10.1186/s40677-016-0041-1, 2016.

949 Hedges, S.B., Cohen, W.B., Timyan, J., and Yang, Z.: Haiti's biodiversity threatened by nearly complete
950 loss of primary forest, *Proc. Nat. Ac. Sc.*, 115(46), 11850–11855, doi: 10.1073/pnas.1809753115, 2018.

951 Kargel, J., Leonard, G., Shugar, D., Haritashya, U., Bevington, A., Fielding, E., Fujita, K., Geertsema,
952 M., Miles, E., Steiner, J., Anderson, E., Bajracharya, S., Bawden, G., Breashears, D., Byers, A., Collins,
953 B., Dhital, M., Donnellan, A., Evans, T., Geai, M., Glasscoe, M., Green, D., Gurung, D., Heijnen, R.,
954 Hilborn, A., Hudnut, K., Huyck, C., Immerzeel, W., Liming, J., Jibson, R., Käab, A., Khanal, N.,
955 Kirschbaum, D., Kraaijenbrink, P., Lamsal, D., Shiyin, L., Mingyang, L., McKinney, D., Nahirnack, N.,
956 Zhuotong, N., Ojha, S., Olsenholler, J., Painter, T., Pleasants, M., Pratima, K., Yuan, Q., Raup, B., Regmi,
957 D., Rounce, D., Sakai, A., Donghui, S., Shea, J., Shrestha, A., Shukla, A., Stumm, D., Kooij, M. van der,
958 Voss, K., Xin, W., Weihs, B., Wolfe, D., Lizong, W., Xiaojun, Y., Yoder, M., and Young, N.: Geomorphic

959 and geologic controls of geohazards induced by Nepal's 2015 Gorkha earthquake, *Science*, 351,
960 doi:10.1126/science.aac8353, 2016.

961 Keefer, D.K., and Wilson, R.C.: Predicting earthquake-induced landslides, with emphasis on arid and
962 semi-arid environments, In *Landslides in a Semi-arid environment* (Inland Geological Society, Sadler
963 and Morton, eds.), 2, 118–149, 1989.

964 Lacroix, P.: Landslides triggered by the Gorkha earthquake in the Langtang valley, volumes and initiation
965 processes, *Earth Planets Space*, 68(46), 10 p., doi: 10.1186/s40623-016-0423-3, 2016.

966 Lemaire, E., Mreyen, A.-S., Dufresne, A., and Havenith, H.-B.: Analysis of the influence of structural
967 geology on the massive seismic slope failure potential supported by numerical modelling. *Geosciences*,
968 10(8), 323, 30 p., doi:10.3390/geosciences10080323, 2020.

969 Malamud, B. D., Turcotte, D. L., Guzzetti, F., and Reichenbach, P.: Landslide inventories and their
970 statistical properties, 29, 687–711, doi:10.1002/esp.1064, 2004.

971 Marc, O., Meunier, P., and Hovius, N.: Prediction of the area affected by earthquake-induced landsliding
972 based on seismological parameters, *Nat. Hazards Earth Sys.*, 17, 1159–1175, doi:10.5194/nhess-17-
973 1159-2017, 2017.

974 Martinez, S.N., Allstadt, K.E., Slaughter, S.L., Schmitt, R., Collins, E., Schaefer, L.N., and Ellison, S.:
975 Landslides triggered by the August 14, 2021, magnitude 7.2 Nippes, Haiti, earthquake, U.S. Geological
976 Survey Open-File Report 2021–1112, 17 p., doi:10.3133/ofr20211112, 2021.

977 Okuwaki, R., and Fan, W.: Oblique convergence causes both thrust and strike-slip ruptures during the
978 2021 M 7.2 Haiti earthquake, *Geoph. Res. Letters*, 49(2), 12 p., doi:10.1029/2021GL096373, 2022.

979 Olson, S., Green, R., Lasley, S., Martin, N., Cox, B., Rathje, E., Bachhuber, J., and French, J.:
980 Documenting Liquefaction and Lateral Spreading Triggered by the 12 January 2010 Haiti Earthquake,
981 *Earthquake Spectra*, 27, 93–116, doi:10.1193/1.3639270, 2011.

982 Parker, R.N., Hancox, G.T., Petley, D.N., Massey, C.I., Densmore, A.L., and Rosser, N.J.: Spatial
983 distributions of earthquake-induced landslides and hillslope preconditioning in the northwest South
984 Island, New Zealand, *Earth Surface Dynamics*, 3 (4), 501–525, doi:10.5194/esurf-3-501-2015, 2015.

985 Petley, D.: Landslides from the 14 August 2021 earthquake in Haiti, On
986 blogs.agu.org/landslideblog/2021/09/03/landslides-from-the-14-august-2021-earthquake-in-haiti, 2021.

987 Poupardin, A., Calais, E., Heinrich, P., Hébert, H., Rodriguez, M., Leroy, S., Aochi, H., and Douilly, R.:
988 Deep submarine landslide contribution to the 2010 Haiti earthquake tsunami, *Nat. Hazards Earth Syst.*
989 *Sci.*, 20, 2055–2065, doi:10.5194/nhess-20-2055-2020, 2020.

990 Saint Fleur, N., Klinger, Y., and Feuillet, N.: Detailed map, displacement, paleoseismology, and
991 segmentation of the Enriquillo-Plantain Garden Fault in Haiti, *Tectonophysics*, 778, 25 p.,
992 doi:10.1016/j.tecto.2020.228368, 2020.

993 Sassa, S., and Takagawa, T.: Liquefied gravity flow-induced tsunami: first evidence and comparison
994 from the 2018 Indonesia Sulawesi earthquake and tsunami disasters, *Landslides*, 16, 195–200,
995 doi:10.1007/s10346-018-1114-x, 2018.

996 Stark, C. P., and Hovius, N.: The characterization of landslide size distributions, *Geoph. Res. Letters*,
997 28(6), 1091–1094, doi:10.1029/2000GL008527, 2001.

998 Stein, R.S., Toda, S., Lin, J., and Sevilgen, V.: Are the 2021 and 2010 Haiti earthquakes part of a
999 progressive sequence? *Temblores*, doi:10.32858/temblor.197, 2021.

1000 Symithe, S. J., Calais, E., Haase, J. S., Freed, A. M., and Douilly, R.: Coseismic Slip Distribution of the
1001 2010 M 7.0 Haiti Earthquake and Resulting Stress Changes on Regional Faults, *Bull. Seis. Soc. Am.*,
1002 103, 2326–2343, doi:10.1785/0120120306, 2013.

1003 Tanyaş, H., Westen, C. J., Allstadt, K. E., Jessee, M. A. N., Görüm, T., Jibson, R. W., Godt, J. W., Sato,
1004 H. P., Schmitt, R. G., Marc, O., and Hovius, N.: Presentation and Analysis of a Worldwide Database of
1005 Earthquake-Induced Landslide Inventories, *J. Geophys. Res. Earth Surf.*, 122, 1991–2015,
1006 doi:10.1002/2017jgf004236, 2017.

1007 Tanyas, H., Rossi, M., Alvioli, M., Westen, C. J. van, and Marchesini, I.: A global slope unit-based
1008 method for the near real-time prediction of earthquake-induced landslides, *Geomorphology*, 327, 126–
1009 146, doi:10.1016/j.geomorph.2018.10.022, 2019a.

1010 Tanyaş, H., Westen, C. J., Allstadt, K. E., and Jibson, R. W.: Factors controlling landslide frequency–area
1011 distributions, *Earth Surf Processes*, 44, 900–917, doi:10.1002/esp.4543, 2019b.

1012 Tanyaş, H., and Lombardo, L.: Variation in landslide-affected area under the control of ground motion
1013 and topography, *Eng. Geol.*, 260, 105229, doi:10.1016/j.enggeo.2019.105229, 2019.

1014 Tanyaş, H., Görüm, T., Fadel, I., Yıldırım, C., and Lombardo, L.: An open dataset for landslides triggered

1015 by the 2016 Mw 7.8 Kaikōura earthquake, New Zealand, *Landslides*, 19, 1405–1420,
1016 doi:10.1007/s10346-022-01869-9, 2022.

1017 Von Hillebrandt-Andrade, C., and Vanacore, E.: Citizen science for studying earthquakes, *Science*, 376,
1018 246–247, <https://doi.org/10.1126/science.abo5378>, 2022.

1019 Wartman, J., Dunham, L., Tiwari, B., and Pradel, D.: Landslides in Eastern Honshu Induced by the 2011
1020 Tohoku Earthquake Landslides in Eastern Honshu Induced by the 2011 Tohoku Earthquake, *Bull. Seis.
1021 Soc. Am.*, 103, 1503–1521, <https://doi.org/10.1785/0120120128>, 2013.

1022 Wilson, R.C., and Keefer, D.K.: Predicting the areal limits of earthquake-induced landsliding, In
1023 *Evaluating Earthquake Hazards in the Los Angeles Region - An Earth Science Perspective* (Ziony, ed.),
1024 U.S. Geol. Surv. Prof. Paper 1360, 316-345, 1985.

1025 Xu, C., Shyu, J. B. H., and Xu, X.: Landslides triggered by the 12 January 2010 Port-au-Prince, Haiti,
1026 Mw = 7.0 earthquake: visual interpretation, inventory compiling, and spatial distribution statistical
1027 analysis, *Nat. Hazards Earth Syst. Sci.*, 14(7), 1789–1818, doi:10.5194/nhess-14-1789-2014, 2014.

1028

1029

1030

1031

1032

1033

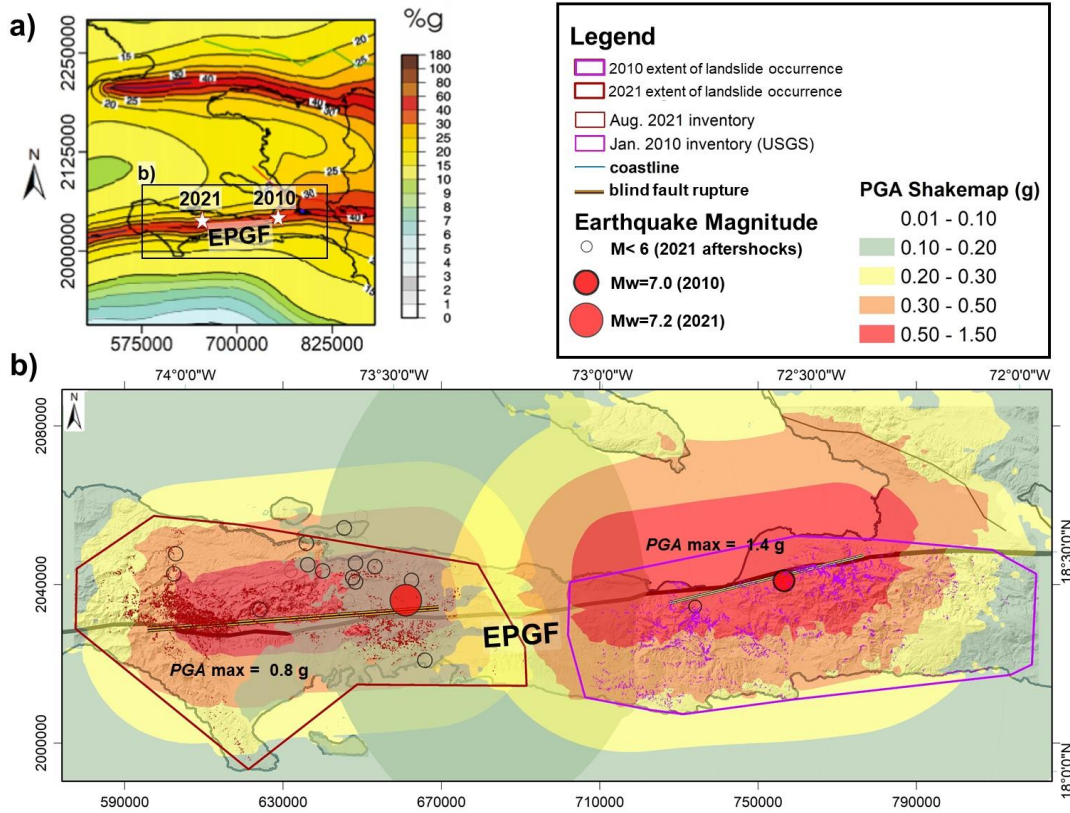
1034

1035

1036

1037

1038



1040

1041 **Figure A1: a) Seismic hazard map of Haiti (modified from Frankel et al., 2011) with location of the January**

1042 **12, 2010, and August 14, 2021, main epicenters. b) Combined overlays of shakemaps of the 2010 (right part**

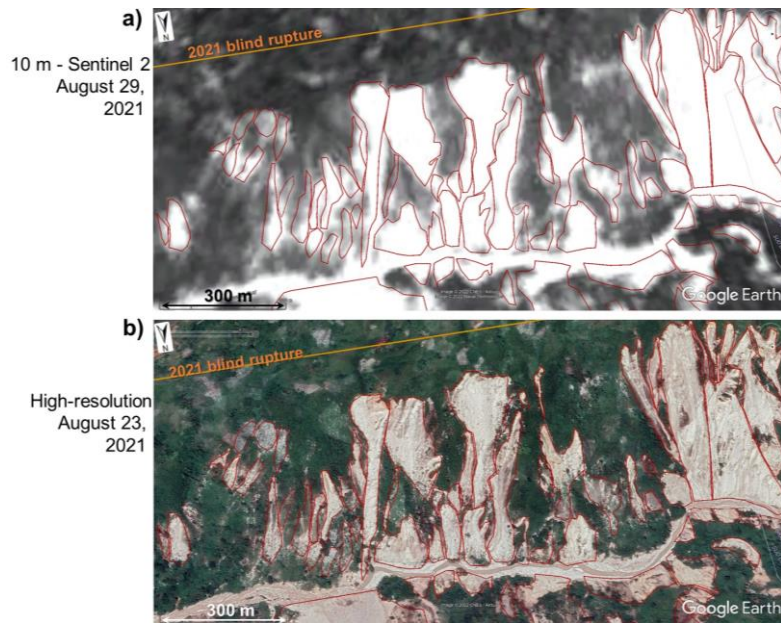
1043 **of map) and 2021 (left part) earthquakes.**

1044

1045

1046

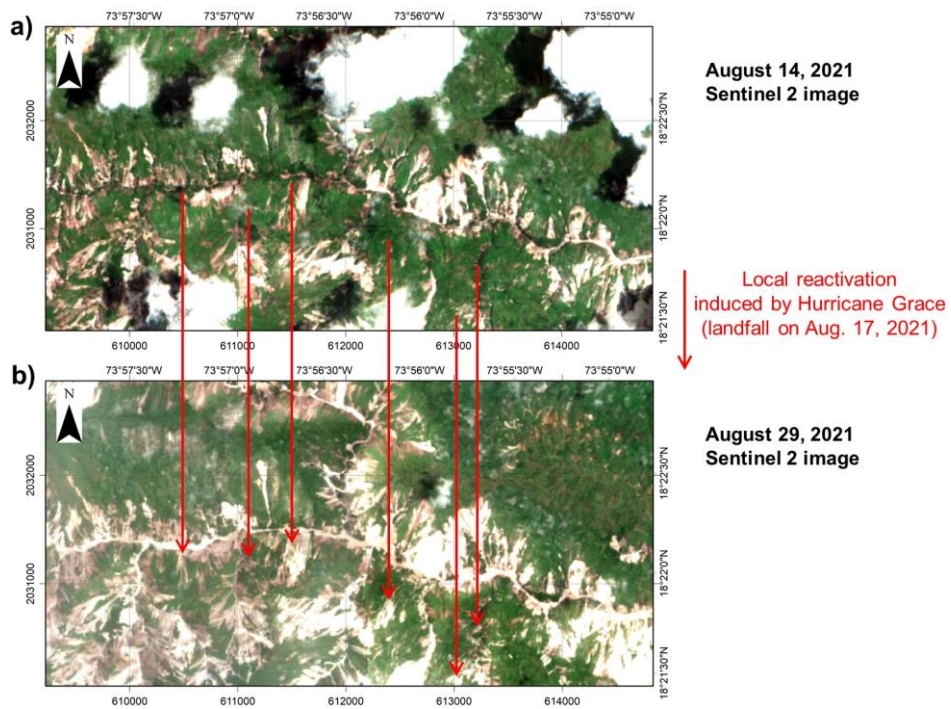
1047



1048

1049 **Figure A2: Comparison between (a) a Sentinel-2 image (10-m resolution) and (b) a high-resolution (~0.5-1 m)**

1050 **image of the same area affected by landslides triggered by the earthquake event in August 2021.**



1051

1052 **Figure A3: Comparison between Sentinel-2 images (10-m resolution) for the same area obtained for (a) August**

1053 **14 (about 2h after the main shock) and for (b) August 28, 2021 (12 days after impact by Hurricane Grace that**

1054 **crossed the region on August 16, 2021). Red arrows point to zones where an intensification of denudation and**

1055 **sliding can be observed.**